



# HHS Public Access

## Author manuscript

*Annu Rev Control.* Author manuscript; available in PMC 2020 January 24.

Author Manuscript

Author Manuscript

Author Manuscript

Author Manuscript

Published in final edited form as:

*Annu Rev Control.* 2019 ; 48: 442–471. doi:10.1016/j.arcontrol.2019.05.002.

## A Review of Electrical Impedance Tomography in Lung Applications: Theory and Algorithms for Absolute Images

**Thiago de Castro Martins<sup>a</sup>, André Kubagawa Sato<sup>a</sup>, Fernando Silva de Moura<sup>b</sup>, Erick Dario León Bueno de Camargo<sup>b</sup>, Olavo Luppi Silva<sup>b</sup>, Tales Batista Rattis Santos<sup>c</sup>, Zhanqi Zhao<sup>d,e</sup>, Knut Möller<sup>d</sup>, Marcelo Brito Passos Amato<sup>f</sup>, Jennifer L. Mueller<sup>g</sup>, Raul Gonzalez Lima<sup>c</sup>, Marcos de Sales Guerra Tsuzuki<sup>a</sup>**

<sup>a</sup>Computational Geometry Laboratory, Escola Politécnica da Universidade de São Paulo, Brazil

<sup>b</sup>Universidade Federal do ABC, Center of Engineering, Modeling and Applied Social Sciences, Brazil

<sup>c</sup>Department of Mechanical Engineering, Escola Politécnica da Universidade de São Paulo, Brazil

<sup>d</sup>Institute of Technical Medicine, Furtwangen University, Germany

<sup>e</sup>Department of Biomedical Engineering, Fourth Military Medical University, Xi'an, China

<sup>f</sup>Respiratory Intensive Care Unit, Pulmonary Division, Hospital das Clínicas, Universidade de São Paulo, Brazil

<sup>g</sup>Department of Mathematics, and School of Biomedical Engineering, Colorado State University, United States of America

### Abstract

Electrical Impedance Tomography (EIT) is under fast development, the present paper is a review of some procedures that are contributing to improve spatial resolution and material properties accuracy, admittivity or impeditivity accuracy. A review of EIT medical applications is presented and they were classified into three broad categories: ARDS patients, obstructive lung diseases and perioperative patients. The use of absolute EIT image may enable the assessment of absolute lung volume, which may significantly improve the clinical acceptance of EIT. The Control Theory, the State Observers more specifically, have a developed theory that can be used for the design and operation of EIT devices. Electrode placement, current injection strategy and electrode electric potential measurements strategy should maximize the number of observable and controllable directions of the state vector space. A non-linear stochastic state observer, the Unscented Kalman Filter, is used directly for the reconstruction of absolute EIT images. Historically, difference images were explored first since they are more stable in the presence of modelling errors. Absolute images require more detailed models of contact impedance, stray capacitance and properly refined finite element mesh where the electric potential gradient is high. Parallelization of the forward

\*Corresponding author: mtsuzuki@usp.br (Marcos de Sales Guerra Tsuzuki).

**Publisher's Disclaimer:** This is a PDF file of an unedited manuscript that has been accepted for publication. As a service to our customers we are providing this early version of the manuscript. The manuscript will undergo copyediting, typesetting, and review of the resulting proof before it is published in its final citable form. Please note that during the production process errors may be discovered which could affect the content, and all legal disclaimers that apply to the journal pertain.

program computation is necessary since the solution of the inverse problem often requires frequent solutions of the forward problem. Several reconstruction algorithms benefit by the Bayesian inverse problem approach and the concept of prior information. Anatomic and physiologic information are used to form the prior information. An already tested methodology is presented to build the prior probability density function using an ensemble of CT scans and in vivo impedance measurements. Eight absolute EIT image algorithms are presented.

## Keywords

Electrical Impedance Tomography; Anatomical Atlas; Bayesian Inference; Massive Parallel Computing; Approximation Error; ARDS; Lung Diseases

## 1. Introduction

Recently, non-invasive medical image techniques emerged, and currently play a crucial role in different clinical applications [1]. One of the promising techniques is Electrical Impedance Tomography (EIT), which is a noninvasive internal impeditivity reconstruction technique for measurements to be performed on the body surface. Usually, alternated current at a single frequency is injected through electrodes, and the electric potential is measured on the same electrodes. It is possible to inject current at multiple frequencies [2], and to impose electric potentials on electrodes and measure the current generated.

The images obtained from EIT can be classified as absolute and difference images. Difference EIT includes frequency-difference [3, 4] and time-difference [5, 6]. Time-difference images [7, 8] are commercially available and these devices determine changes in the internal impeditivity with respect to a reference impeditivity distribution. Absolute images are much more difficult to obtain and are prone to present artifacts mainly due to modelling errors. Moreover, they require more advanced numerical algorithms for the reconstruction and, therefore, have higher computational requirements.

Even though the spatial resolution of EIT is low when compared to other imaging techniques such as computerized tomography, magnetic resonance, or ultrasonic imaging, EIT has important advantages. It is a low cost, portable and non-radioactive imaging technique with fast time-response characteristics. EIT has several practical applications in medicine, which include, but are not limited to: detection of breast cancer [9] and acute cerebral stroke [10], cardiac activity monitoring [11] and forced lung aeration by mechanical ventilation in critically ill patients [12, 13]. The latter application is the focus of the work proposed in this paper. This paper presents a complete review of thorax imaging using time-difference EIT in Section 6. Despite the large number of applications of time-difference EIT, absolute imaging through EIT is a promising technique [14, 15].

A review of EIT lung applications is timely since there is a profusion of theoretical and technological advances that are increasing the spatial resolution and the accuracy of the estimated electrical material properties [16, 17, 18, 19, 20, 21, 22, 23, 24, 25, 26, 27]. Examples of these include the parallelization of the forward problem [17], the use of algorithms that do not require derivatives of the performance index [18, 19], the

regularizations based on anatomy and physiology [23, 28], and the correction of the inversion problem caused by a reduced or simplified model [22]. Furthermore, an increase in image quality is likely to expand the set of medical applications. Some advances are directly related to control theory; for instance, the Unscented Kalman Filter (UKF) algorithm for EIT is a direct application of stochastic control theory. The techniques presented here, including the methodology to build an anatomical atlas, the use of the UKF connected to the approximation error method, the acceleration of the SA, and the parallel D-Bar method with prior information are not widely known.

The text is structured as follows. Section 2 describes the inverse problem with several basic concepts: forward problem, current patterns, the finite element model (FEM) and the electrode model. The forward model is evaluated several times by iterative inversion methods (thus, with the exception of the D-Bar method) and must be processed as fast as possible. For this, a section on massive parallelization acceleration based on GPGPU is presented, which is shown to be much faster than CUDA cuBLAS from Nvidia. Section 3 presents how to approach EIT with the control theory. We explain that the current injections can be associated with controllability and measured electric potentials with observability. Section 4 describes the Bayesian approach to EIT and the application of the approximation error method to include errors from the model in the formalization. Section 5 presents eight different methods for absolute image determination. Five of the methods presented are based on simulated annealing and the three remaining methods are deterministic approaches. Section 6 presents a complete review of thoracic EIT imaging using time-difference EIT. Section 7 presents a discussion comparing the presented reconstruction methods. It is concluded that despite the large number of applications of time-difference EIT, absolute imaging through EIT is a promising technique [14, 15]. Some conclusions are drawn in Section 8.

## 2. The Inverse Problem

The EIT is an inverse problem, and all the methods reviewed here (except the D-Bar) have similar building blocks to solve the inverse problem iteratively, as shown in Fig. 1. The potential measurements are the input. An initial conductivity distribution is given, and the main body of the solution method is an iterative loop in which the forward problem is evaluated, the measured potentials are compared with the simulated potentials, and if they are within the specified tolerance, the program is terminated. If not, the conductivity distribution is updated, and a new iteration begins. The forward problem is evaluated using massive parallelization with GPGPU and has as input the current patterns, FEM, electrode model, and the conductivity distribution. The output is the potential at the electrodes which are used to evaluate the objective function. Note that the SA-based methods verify whether the solution is accepted or not before the convergence check, while the G-N and UKF methods always accept the solution. The D-Bar method is much simpler: given the potential 125 measurements it directly computes the conductivity distribution.

## 2.1. The Forward Problem

The forward EIT problem can be described as the determination of the electric potential distribution  $\phi$  in the domain represented by the generalized Laplace equation, given the conductivity distribution  $\sigma$  inside the domain and the current  $J$  injected through the boundary [16]. The generalized elliptic equation, defined by

$$\nabla \cdot (\sigma \nabla \phi) = 0, \quad (1)$$

with the boundary condition

$$\sigma \frac{\partial \phi}{\partial \hat{n}} = J, \quad (2)$$

where  $\hat{n}$  is the external normal, are a simplification of the Maxwell's equations under the hypothesis that the excitation frequencies are low and a quasi-static approximation holds true. Of particular interest are the potentials at the electrodes, which are frequently the measured values for solving the inverse problem. The building blocks to implement the forward problem are shown in Fig. 2.

## 2.2. Current Patterns

As previously explained, current is injected at specific points of the domain boundary (the electrodes). Most EIT systems perform current injection through a pair of electrodes, using a bipolar current source [12, 29, 30, 18, 26]. Some systems implement current injection through multiple electrodes [31, 32, 33]. We here focus on bipolar current application through pairs of electrodes, whereby the two injecting electrodes are separated by  $q$  electrodes, referred to as a *skip-q* current pattern. A full set of measurements is obtained by applying current repeatedly and sequentially to generate a linearly independent set of measurements.

## 2.3. Finite Element Model

The forward EIT problem described by the elliptic equation (1) with boundary conditions (2) does not have a known analytical solution for an irregular domain and isotropic media. Therefore, a common approach is to numerically solve the partial differential equation (PDE) using the finite element method (FEM).

In the FEM, a linear system can be derived for the elements either through the Weighted Residual Method or a Variational formulation. Combining all elements, the resulting formulation is given by

$$K(\sigma) \cdot \phi_i^q = j_i^q, \quad (3)$$

where  $K(\sigma) \in \mathbb{C}^{n \times n}$  is the conductivity matrix calculated given the conductivity distribution  $\sigma$ ,  $n$  is the number of mesh nodes,  $q$  denotes the number of electrodes skip between a pair of injecting electrodes,  $N$  is the total number of electrodes,  $j_i^q \in \mathbb{C}^n$  contains the imposed current at the  $i$ -th and  $(i + q + 1 \bmod N)$ -th electrodes (*skip-q* current pattern) and  $\phi_i^q \in \mathbb{C}^n$

are the measured potentials at each electrode. The indices in  $\phi_i^q$  represent the specific current pattern  $j_i^q$  used when the potentials were measured.

#### 2.4. Electrode models

Measurements in lung EIT are typically collected by electrodes attached around the chest, usually with a conductive gel layer between the skin and the metallic electrodes. Since human body is considered as an electrolyte, i.e. ions are the charge carriers of electric current, the EIT electrode is the site where the electronic current is transduced to ionic current. Several authors have observed an impedance at the electrode-electrolyte interface when measuring bioelectric events [34, 35]. Although this is a complex phenomena and many models have been proposed at atomic scale [36], in EIT measurements we can assume that the electric potential is discontinuous at the skin-electrode interface, which is frequently referred to as the *contact impedance*.

Additionally, the current density distribution is not uniform over the electrode [37] (edge effect) and part of the injected current may run near the boundary (skin) to the adjacent electrode (shunt effect). Cheng et al. [38] was the first to introduce a set of boundary conditions to account for these three effects (edge, shunt and contact impedance) and the gaps between electrodes. Although other models have been proposed, such as the Point Electrode Model (PEM) [39], the Gap Model (GM), and the Shunt Electrode Model (SEM) [40]; the model proposed by Cheng et al. [38] is the most comprehensive and is referred to as the *Complete Electrode Model* (CEM).

The existence and uniqueness of a solution to the PDE with the CEM was proved by Somersalo et al. [41], and it was implemented with the FEM using a 2D mesh of linear triangular elements in [42]. Hua et al. [13] derived a local conductivity matrix for the FE electrode where its width is much larger than its thickness and concluded that with this simplification the model depends on a single parameter proportional to  $\rho t$ , where  $t$  is the thickness and  $\rho$  is the resistivity associated with skin-electrode interface. Vauhkonen et al. [43] implemented CEM for a 3D domain using first and second order basis functions.

Since in a clinical setting it is difficult that electrode-skin contact remains stable, contact impedance may vary over time. Vilhunen et al. [44] introduced the theory for simultaneous imaging and estimation of contact impedances. However, [45], reported that if contact impedance is very close to zero one should experience numerical instabilities in making such simultaneous estimation. One way to circumvent this problem is to replace CEM by the Shunt Model. A rigorous proof that CEM converge to SEM was presented by [46]. The other way is to use the “smoothened” version of CEM proposed by [47] that makes the numerical convergence easier when estimating the image simultaneously with electrode locations and/or contact conductances.

Zhang and Li [48] proposed a modification to CEM, named *Instrumental Electrode Model* (*IEM*) which considers instrumental loading effects of measurement hardware such as output impedance of current sources, input impedance of measurement devices and parasitic capacitance of cables, connectors and electrodes. IEM formulation can provide more

accurate solution for the forward problem in the frequency range from 500 kHz to a few MHz.

**2.4.1. Single, dual and multi-layer electrode models**—A multi-layer electrode model (see Fig. 3) was proposed by Silva [49] and its numerical convergence was studied in [50]. The purpose of a multi-layer electrode model is to simulate by the FEM, the discontinuous electric potential drop at the interface due to the contact impedance. At the most external layer (metallic layer in Fig. 3a) it is attributed the resistivity of the metallic wire, while at the interface layer, an equivalent uniform resistivity can be attributed to match (a possibly measured) contact impedance. In the forward problem, contact impedance can be measured and its equivalent resistivity attributed to interface layer, while in inverse problem, contact impedance can be estimated simultaneously with domain impedance with the methods proposed in [44]. The concept of multilayer electrode model was also applied for 2D domain in [51, 52]. In this case, the outermost nodes are short-circuited, i.e. same electric potential are imposed (see Fig. 4).

The top panel of Fig. 3b depicts the phenomena of contact impedance. We consider that the electrode is the part of metallic wire which is in contact with the domain, whose voltage is constant with respect to a reference. The electrode voltage at the right (metallic side) is different from the voltage at the left (domain side) by  $V_Z$ . The product of electrode current  $I_e$  with  $V_Z$  is the contact impedance  $Z$ . In electrode models whose FEM implementation is based on a super-element, such as in Hua et al. [13], electric potential representation is constrained the order of the interpolation function polynomial. Then the order must be high enough to represent a steep voltage variation in a single super-element.

The bottom panel of Fig. 3b is a radial section cut of the mesh in Fig. 3a. Two blocks (interface and metallic layer) are introduced with hundreds of tetrahedrons. Since the implementation of a multi-layer electrode model is similar to PEM, electric potential distribution is not accurate near current injection node because at this point current density is virtually infinite. However, we believe that as long it gets closer to the boundary of the domain of interest, it converges to the real value. This model, with a sufficiently refined mesh, can be used to represent a non-approximated model  $h(\sigma)$  in Approximation Error Method (Sec. 4.1, [49]).

## 2.5. Massive Parallelization Acceleration

The forward EIT problem solution adopted herein consists in solving a set of linear systems (see eq. (3)). A conjugate-gradient (CG) algorithm, which involves a series of matrix and vector operations, is employed as a numerical solver. These operations are usually suitable for parallel implementation, as many calculations can be concurrently processed. A massive parallelization can be obtained through a GPGPU (general purpose graphics processing unit) operating on a large number of cores. Moreover, a very high computational cost may be required for the EIT problem when a refined mesh is adopted for the FEM. Thus, employing massive GPU parallelization may be advantageous for the EIT solution proposed herein, as it depends on the performance of the forward problem solver.

The preconditioned CG algorithm involves matrix-vector multiplication and a triangular solver. A GPU accelerated variant can be constructed by efficiently parallelizing these operations by using sparse matrix representations. Furthermore, the vector operations can also be implemented in the GPU without special storage formats.

GPU implementations are capable of achieving very high speedups by using a large number of cores. Nevertheless, due to the characteristics of GPGPUs, the algorithm performance is hindered by thread divergence and uncoalesced memory access, which are common occurrences when adopting conventional sparse matrix representations. Therefore, several sparse matrix storage solutions were proposed in the literature, of which the padded jagged diagonal storage (pJDS) [53] is chosen as a good compromise between memory usage and performance.

The pJDS improves upon the ELLPACK-R [54] format, consisting of two matrices and one vector, as shown in Fig. 5. Firstly, all rows are compressed by shifting non-zero elements to the left. Then the data matrix *val* is determined by zero-padding the result and the column matrix *col\_idx* contains the corresponding column of each element. Finally, the vector *rowsize* contains the number of non-zeros for each row. Algorithm 1 shows the sparse vector-matrix multiplication (spMVM) kernel for the ELLPACK-R format, where *n* is the size of original matrix, *rhs* is the multiplying vector and *c* stores the result.

As observed from the example, some zero values are not eliminated by the ELLPACK-R. Thus, the pJDS storage was proposed to reduce the size of the ELLPACK-R matrix. Initially, the rows of the ELLPACK value matrix are reordered according to the number of non-zeros (see Fig. 6a). Then, the rows are divided into successive blocks of fixed size and padded within its block. As the memory is coalesced into multiples of the warp size in the GPU, the blocks are set to this size. The *val* and *col\_idx* matrices are converted into 3 vectors, including an auxiliary vector containing the columns offsets (*col\_start*, as shown in Fig 6b). A permutation vector is also required to recover the initial row ordering. The spMVM algorithm for the cpJDS format is given by Algorithm 2.

#### Algorithm 1

##### ELLPACK-R spMVM

---

```

c[1:n]= 0;
for i = 1:n do
    for j = 1:rowsize[i] do
        c[i] += val[i,j] * rhs[col_idx[i,j]];
    end for
end for

```

---

The triangular solver cannot be directly parallelized using backward/forward substitution, as there are dependencies between variables. Fig. 7a shows a lower triangular matrix generated from a simple FEM model in which each variable must be determined sequentially. A coloring scheme and subsequent reordering can be applied to the matrix in order to reduce the dependencies, as shown in Fig. 7b. In the example case, only two colors are used,

indicating that the solution can be obtained by a sequence of two parallel blocks. Tavares et al. [17] incorporated the coloring pre-processing to the sparse matrix format, creating the colored pJDS (cpJDS) storage. Fig. 8 shows the conversion from the ELLPACK-R to the cpJDS format, starting with the coloring scheme. Then, the rows are sorted according to the color, then to the number of non-zero elements. Padding is added to each row and color group according to the warp size. Finally, the diagonal elements are moved to the beginning of each row to facilitate the backward/forward substitution algorithm. The lower triangle solver is given by Algorithm 3, in which the inner loop is the kernel for the GPU massive parallelization.

### Algorithm 2

pJDS spMVM

---

```
c[1:n]= 0;
for i = 1:n do
    for j = 1:rowsize[i] do
        col_offset = col_start[i];
        c[permvec[i]] += val[col_offset+j] * rhs[col_idx[col_offset+j]];
    end for
end for
```

---

### Algorithm 3

cpJDS lower triangular solver

---

```
for k = 1:ncolors do
    color_offset = color_start[k];
    nrows = color_start[k+1] - color_start[k];
    for i = 1:nrows do sumrow = rhs[col_idx[col_offset]];
        for j = 1:rowsize[color_offset+i] do
            col_offset = col_start[color_offset + i];
            sumrow -= val[col_offset+j] * c[permvec[[col_idx[col_offset+j]]];
        end for
        c[permvec[i]] = sumrow / col_start[color_offset];
    end for
end for
```

---

The parallelized CG was implemented in CUDA, an application programming interface model created by Nvidia, to solve the forward EIT problem. It was tested against two other solutions: a pure serial CG solver and the algorithm provided by the cuBLAS library, developed by Nvidia. A model of a circular recipient filled with a saline solution was created and 32 electrodes were placed around the domain. For each experiment, a sequence of 32 current injections were simulated using a skip-3 pattern and the average execution time for each injection was computed. The results are shown in Fig. 9. The graph shows that the proposed cpJDS based algorithm performed better than the other implementations, specially for larger linear systems. When compared with the serial and cuBLAS solutions, the number

of nodes are observed to have a smaller impact on the execution time of the proposed parallel solver.

### 3. Control Theory Applied to EIT

The EIT inverse problem is often stated as: “*given the excitation current patterns, the model structure, and corresponding electric potentials measured at the boundary surface, estimate the distribution of admittivity inside the domain*”. The following is a representation of this statement

$$\phi_{\partial\Omega} \rightarrow \sigma \quad (4)$$

where  $\phi_{\partial\Omega}$  denotes the electric potential measurements at the boundary of the domain  $\Omega$ . The inverse problem can be decomposed into two inverse problems in series,

$$\phi_{\partial\Omega} \rightarrow \phi_{\Omega} \rightarrow \sigma \quad (5)$$

where  $\phi_{\Omega}$  denotes electric potentials inside the domain  $\Omega$ . The advantage of breaking the inverse problem in two, is that the first inverse problem is linear and the electric potential in the domain can be considered a state vector of a linear system. The second inverse problem, although nonlinear, is well conditioned. It is equivalent to estimating  $\sigma$  with the knowledge of a large number of electric potentials distributed inside the domain. The first inverse problem can take advantage of the theory of state observers of linear systems [26]. The placement of the sensors and actuators can be optimized to maximize the number of observable modes.

According to eq. (3), the finite element model defines an observation model,

$$\phi_i^q = K^{-1}(\sigma) j_i^q. \quad (6)$$

The state space representation of a linear time invariant system in discrete time is represented by [55]

$$x(k+1) = Gx(k) + Hu(k), \quad (7)$$

where state  $x(k)$  can represent electric potential inside the domain  $\phi_{\Omega}$ , system matrix  $G$  is the evolution matrix, excitation vector  $u(k)$  is the current injection pattern  $j_i^q$ , and excitation matrix  $H$  is the inverse of the finite element conductivity matrix  $K(\sigma)$ .

Matrix  $C$  establishes an instantaneous relation between state vector  $x$  and observed vector  $y$ :  $y = Cx$ . Frequently, only a small part of the state vector is measured.

When state vector  $x$  represents the electric potential in the domain  $\phi_{\Omega}$  and the observed vector  $y$  represents the electric potential at the boundary  $\phi_{\partial\Omega}$ , matrix  $C$  becomes a rectangular matrix, with a few non-zero elements in its diagonal and zero off-diagonal elements. Since matrices  $G$ ,  $H$  and  $C$  are all defined in physical terms in (7), the EIT state

space model is known and linear Control Theory applies. The observability matrix [55] is given by,

$$O = [C \ CG \ \dots \ CG^{n-1}]^T, \quad (8)$$

and the controllability matrix is given by

$$P = [H \ GH \ \dots \ G^{n-1}H]. \quad (9)$$

When the data acquisition of all the current injection patterns is conducted much faster than the system evolution, the discrete time evolution matrix  $G$  is approximately the identity matrix  $I$ , and the rank of  $O$  becomes the rank of  $C$  and, similarly, the rank of  $P$  becomes the rank of  $H$  [26]. Therefore, matrix  $C$  operates as observability and matrix  $H$  operates as controllability.

The relationship between the observations vector and the state vector is defined by

$$y(k) = Cx(k) = Ox(k). \quad (10)$$

Also, the relationship between state and control vector is defined by

$$x(k) = Hu(k) = Pu(k). \quad (11)$$

Substituting eq. (11) into eq. (10) reveals that the transconductance matrix  $\Gamma$ , the matrix that maps  $u(k)$  to  $y(k)$  can be decomposed as observability times controllability,

$$y(k) = OPu(k). \quad (12)$$

Therefore, the vector space spanned by vectors  $y(k)$  is reduced by any controllability or observability rank deficiency. The same transconductance matrix  $\Gamma$  can be SVD decomposed,

$$y(k) = U\Sigma V^T u(k). \quad (13)$$

One particular realization of the linear system is the internally balanced system [56], which has observability,

$$O = U\Sigma^{1/2}, \quad (14)$$

and has controllability

$$P = \Sigma^{1/2}V^T. \quad (15)$$

The singular values, the diagonal values of  $\Sigma$ , are observability indexes and controllability indexes. Modifications of electrode placement, current injection strategy, measurement strategy and/or electrode design that maximize the number of singular values larger than the noise variance improve the quality of the images [26]. The number of singular values above

the noise variance constitutes a design criterion for EIT hardware design, excitation strategy and measurement strategy.

Figure 10 is a comparison of EIT reconstructions of a cylindrical 3D numerical phantom with one object. The current injection skip and differential measurement skip is equal for each of the four numerical phantoms. The larger the number of singular values above the noise level, the better the image. The best images are skip 6 and skip 14. The last image, skip 15, has a rank deficient observability matrix, two objects appear in the image, whereas only one object is in the phantom.

#### 4. The Bayesian Approach to the Inverse Problem

While forward EIT solutions can be readily computed, the inverse problem, that is, reconstruction of conductivity distribution is severely ill-conditioned. A Bayesian approach leads to the reconstruction of maximum *a posteriori* (MAP) likelihood solutions [23, Sec. 3.1.1].

The electric potentials can be computed from eq. (3). Given a conductivity distribution  $\sigma$  and an applied current  $j_i^q$  the forward problem solution obtains the vector of potentials *expected* from a numerical model  $\phi_{i,e}^q$  (indicated by subscript  $e$ )

$$\phi_{i,e}^q(\sigma) = K(\sigma)^{-1} j_i^q. \quad (16)$$

Let  $\phi_{i,e}^q$  be the expected potentials at the electrodes. A model for *measured* electric potentials  $\phi_{i,m}^q = \phi_{i,e}^q(\sigma) + e$  is obtained, where  $e$  is a random error vector. If  $P(e)$  is the probability density function for random error  $e$ , then the probability of a given measure  $\phi_{i,m}^q$  given a conductivity distribution  $\sigma$  for a single  $j_i^q$  is

$$\pi(\phi_{i,m}^q | \sigma) = P(\phi_{i,m}^q - \phi_{i,e}^q(\sigma)).$$

EIT uses surface measurements for several current patterns. Let  $N$  be the number of different injection patterns,  $j_i^q$ ,  $\phi_{i,m}^q$  denotes measured electric potentials,  $\phi_{i,e}^q(\sigma)$  denotes expected electric potentials for the  $i$ -th injected current, and  $\mathcal{M} = \{\phi_{1,m}^q, \dots, \phi_{N,m}^q\}$  is the *the ensemble* of measured potentials; hence, its probability distribution given  $\sigma$  is

$$\pi(\mathcal{M} | \sigma) = \prod_{i=1}^N P(\phi_{i,m}^q - \phi_{i,e}^q(\sigma)). \quad (17)$$

By taking  $\pi(\sigma)$  as a *prior* distribution for  $\sigma$ , then from Bayes' rule [20, 21],

$$\pi(\sigma | \mathcal{M}) \propto \pi(\sigma) \prod_{i=1}^N P(\phi_{i,m}^q - \phi_{i,x}^q(\sigma)). \quad (18)$$

A MAP estimate for conductivity distribution  $\tilde{\sigma}$  is one that maximizes (18). By supposing the distribution of errors  $e$  as independent, Gaussian, centered around zero and with covariance matrix  $\Omega$ , such that  $\Omega^{-1} = L^t L$ ,

$$\tilde{\sigma} = \arg \min_{\sigma} \sum_{i=1}^N \|L(\phi_{i,m}^q - \phi_{i,e}^q(\sigma))\|^2 + R(\sigma) \quad (19)$$

where  $R(\sigma) \propto \ln \pi(\sigma)$  is the *regularization* term, related to the *prior* knowledge of  $\sigma$ . Therefore, from (19), under Gaussian assumptions, the likelihood probability density function is quadratic.

A more explicit form of the posterior probability density function, under Gaussian assumptions, and prior information of  $\sigma \sim \mathcal{N}(\sigma_0, \Gamma)$ , is given by

$$\pi(\sigma | \mathcal{M}) \propto e^{-\frac{1}{2}(\phi_m^q - \phi_e^q(\sigma))^T \Omega^{-1} (\phi_m^q - \phi_e^q(\sigma)) - \frac{1}{2}(\sigma - \sigma_0)^T \Gamma^{-1} (\sigma - \sigma_0)} \quad (20)$$

#### 4.1. Approximation Error Method

The use of a reduced or an approximated model in the inverse problem leads to image quality problems, unless the statement of the inverse problem is improved. A method for the improvement of the definition of the inverse problem is called the Approximation Error Method [22, 57, 58].

Considerations of computational power and memory requirements often result in the use of simplified or approximated models for solving the inverse problem. The approximated model will be denoted by  $h^*(\sigma^*)$  and a nonapproximated model will be denoted by  $h(\sigma)$ . Assume it is known the prior distribution of the random variable vector  $\sigma \sim \mathcal{N}(\sigma_0, \Lambda_{pr})$ . Let us admit that eq. (16) additionally represents the measurement additive noise with the vector of random variables  $w_i$ ,

$$\phi_{i,m}^q(\sigma) = K(\sigma)^{-1} j_i^q + w_i. \quad (21)$$

A representation, of eq. (21), taking into account all the injecting current patterns and a non-approximated model becomes,

$$\phi(\sigma) = h(\sigma) + w. \quad (22)$$

It proves helpful to add and to subtract vector  $h^*(\sigma^*)$ ,

$$\phi(\sigma) = h^*(\sigma^*) + h(\sigma) - h^*(\sigma^*) + w. \quad (23)$$

The last three terms of eq. (23) could represent a new noise vector of random variables,  $w^*$ ; the measured electric potentials are represented by,

$$\phi(\sigma) = h^*(\sigma^*) + w^*. \quad (24)$$

Neglecting the difference of the noise distributions,  $w$  and  $w^*$  represent an inversion crime [23] and deteriorates image quality. The new expected value  $w_0^*$  and covariance  $\Lambda^*$  of  $W^*$ , which is a vector of random variables representing the noise realization vector  $w^*$ , can be computed by

$$w_0^* = E\{W^*\} = E\{h(\sigma) - h^*(\sigma^*) + W\}, \quad (25)$$

where  $W$  is a vector of random variables representing noise realization vector  $w$  and

$$\Lambda^* = E\{(W^* - w_0^*)(W^* - w_0^*)^T\} \quad (26)$$

To more clearly show the difference of the distributions of  $W$  and  $W^*$ , let us assume that the map  $h(\sigma) = H\sigma$  and that  $h^*(\sigma^*) = H\sigma^*$ . There exists a linear operator that converts  $\sigma$  from a refined FE mesh into  $\sigma^*$  from a coarse FE mesh,

$$\sigma^* = P\sigma. \quad (27)$$

Under the simplifying assumption of linearity of  $h(\sigma)$ , the expected value of the enhanced noise, eq. (25), becomes [23],

$$\omega^* = (H - H^*P)\sigma_0 \quad (28)$$

and the covariance of the enhanced noise, eq. (26), becomes [23],

$$\Lambda^* = (H - H^*P)\Lambda_{pr}(H - H^*P)^T + \Lambda_w, \quad (29)$$

therefore, the development of a detailed and refined model to represent  $h(\sigma)$  enables the estimation of the distribution of  $W^*$ , which is different from distribution  $W$  and its use improves the quality of the solution of the inverse problem.

## 5. Methods for Absolute Image Determination

In this section, a total of eight methods for absolute image reconstruction using electrical impedance tomography are presented. Five of the methods are based on SA and are considered probabilistic methods with no dependence on a starting solution. The remaining three methods are deterministic in the sense that for a given measured data and given prior information, the solution will always be the same. The Gauss-Newton method (G-N) is based on a start solution (initial guess) and uses G-N iterations to search for a MAP Probability and is classified as a Bayesian Inversion method. The UKF is a non-linear stochastic state observer of a dynamic system, it is an example of the use of Control Theory in EIT. The D-Bar method is a non-iterative solution method of the nonlinear inverse

problem of an elliptical PDE with known Dirichlet-to-Neumann (DN) map at the boundary and unknown admittivity distribution.

The first SA-based method uses expression (19) as an objective function, and an interesting convergence behavior emerged: an outside-in convergence property. This method is strongly based on the CG methods and it is here called SA-CG. The second SA-based method uses a new objective function whereby the model error is represented. This method is strongly based on the Lanczos Bidiagonalization II algorithm and it is called SA-LB. Both approaches are shown to be complementary. At initial iterations, the SA-CG has lower computational cost and, at later iterations, the SA-LB has lower computational cost. This, motivated the third SA-based method which combines the SA-CG and the SA-LB. The fourth SA-based method is based on the Markov Chain Monte Carlo (MCMC) method, as it is here shown to determine the standard variance of the solution.

All of the proposed methods minimize the error related to the proposed mathematical model using a regularization term. The definition of how the regularization and the original objective function are combined is a hard task. As a first approach, it is better to consider the problem as a multi-objective one and then determine how both functions are combined. The fifth SA-based method is related to this approach.

A G-N algorithm is presented. In the present work the Bayesian Inversion approach is used to form the posterior probability density function of conductivity distribution such that the electrical potential in the boundaries are known. The search for the maximal posterior probability with respect to the conductivity distribution using G-N iteration defines the G-N algorithm. A novel prior information based on anatomy and on physiology of swines is described.

Next, a dual estimation UKF algorithm is presented. Kalman filters are convenient and computationally efficient Bayesian methods to estimate the state of a system when modeling errors are present or model simplifications must be employed. The proposed algorithm uses an UKF to estimate the state  $\sigma$  from (20) at the same time that a parallel UKF is used to adjust the parameters of a nonlinear multi-compartmental evolution model of the lungs during ventilation. The D-Bar Method began as a numerical implementation [59] of the constructive proof of existence and uniqueness of the solution of the 2D generalized Laplace equation, when the boundary DN conditions are known, and the conductivity distribution is sought. The proof of existence and uniqueness of this problem was presented by Nachman [60].

### 5.1. Optimization by Intervalar Simulated Annealing - SA-CG method

The problem in (19) can be simplified to

$$\tilde{\sigma} = \arg \min_{\sigma} \sum_{i,j=1}^N \|(\phi_{i,m}^q[j] - \phi_{i,e}^q(\sigma)[j])\|^2 + R(\sigma) \quad (30)$$

which is non-linear and, for generic regularization terms, non-convex. Nonconvex optimization meta heuristics such as SA are often computationally too expensive for such

problems, as its objective function evaluations are costly. Martins et al. [18, 61], Martins and Tsuzuki [62] proposed a *partial evaluation* of objective function  $E$  at each SA iteration. An estimate  $\tilde{E}$  of  $E$  and the interval boundaries  $E_{\min}$  and  $E_{\max}$  are obtained, such that  $\tilde{E} \in [E_{\min}, E_{\max}]$ . The estimate variation and boundaries variations,  $\Delta\tilde{E}$ ,  $E_{\min}$ ,  $E_{\max}$ , are determined. For a given iteration, if

$$P_{err} \geq \min(e^{-\Delta\tilde{E}/kt}, 1) - \min(e^{-\Delta E_{\max}/kt}, 1) \quad (31)$$

$$P_{err} \geq \min(e^{-\Delta E_{\min}/kt}, 1) - \min(e^{-\Delta\tilde{E}/kt}, 1) \quad (32)$$

are satisfied, then the probability of the SA-CG deviating of a SA with full objective function evaluation is less than  $P_{err}$ .  $\tilde{E}$ ,  $E_{\max}$  and  $E_{\min}$  are obtained by two separate sets of FEM problems solved with CG (as described in (1)), and an upper limit on the  $L_2$  norm following a technique proposed by Meurant [63] is determined.

Martins et al. [18] showed that the CG  $L_2$  error estimate for a given iteration is obtained a number of iterations later. According to Meurant [63], the  $L_2$  error estimate for the CG monotonically decrease and the  $L_2$  estimate a few iterations earlier is an upper bounding for the  $L_2$  in the current iteration. This method is called SA-CG.

**5.1.1. Outside-in heuristic**—An interesting convergence behavior emerged from the SA-CG: the external layers converged faster than the internal layers, defining an outside-in convergence. This was first tried by Somersalo et al. [64] in which they proposed a layer-stripping algorithm based on the outside-in property which consists of solving the impedance imaging incrementally in a layer-by-layer approach. As the outer impedances are more influenced by the current applied to the boundary, the EIT reconstruction may start at the outside layer and then proceed inwards. The SA with incomplete objective function evaluation is the first stable implementation with this property. Fig. 11 shows the convergence of a SA-CG. A visual inspection of the images indicates that the elements closer to the boundary converge faster, thus reproducing the outside-in property.

Tavares et al. [65] proposed an outside-in heuristic to be used with the SA-CG, herein called SA-CG-OIH. Initially, the mesh is divided into five layers, as shown in Fig. 12. At each iteration, the impedance of a single node is modified to generate a new solution. In the original SA with incomplete objective function evaluation algorithm, each node has equal probability for being chosen. With the outside-in heuristic, one of the layers is selected before determining the node to be modified, which must lay inside the chosen layer. The outside-in property is explored by allowing each layer to have different probabilities for being selected. Then, at every objective function evaluation, a feedback algorithm updates the probabilities of each layer.

The feedback algorithm is responsible for stimulating the convergence of the outer layers before the inner ones. A set of weights  $\mathcal{W} = \{w_1, w_2, \dots, w_l\}$  is defined, where  $l$  is the total

number of layers and  $w_i$  is the weight associated with layer  $i$ . The layers are numbered sequentially, from the outermost to the innermost layer. Set  $\mathcal{W}$  dictates the probability of selecting each layer, which is given by

$$P_j = \frac{w_j}{\sum_{k=1}^l w_k} \quad (33)$$

where  $P_j$  is the probability of layer  $j$ .

Initial weight values are attributed, then, after each objective function evaluation, the weights are modified according to the acceptance or rejection of the new solution. In the former situation, i.e. SA accepted the solution, the weight for the current selected layer is increased by a value  $\Delta$ . Otherwise, the weight decreases by the same amount and  $\Delta$  is added to the immediately inner layer weight.

The outside-in heuristic was implemented using initial values  $\mathcal{W} = \{10000, 1000, 100, 10, 1\}$ , which yield the probabilities  $P = \{90.00\%, 9.00\%, 0.90\%, 0.09\%, 0.01\%\}$  for the layers. Fig. 13 displays the evolution of the layer probabilities during the execution of the SA-CG-OIH. The emergent behavior is compatible with the outside-in property, as the outer layers are the mostly explored at the beginning and the inner layers at the end. An analysis of the average cost function, shown in Fig. 14, indicates that the outside-in contributes to a faster convergence, mainly in the initial temperatures. This conclusion is corroborated by the analyses of the average CG iterations by temperature (see Fig. 15), which displays lower values in the initial exploration phase of the SA. Fig. 16 shows two results from this method: (a) three slices of cucumber in saline solution, and (b) a thorax application.

## 5.2. Total Model Error Minimization - SA-LB method

As mentioned in Section 5.1, the evaluation of (30) with bounded errors is made with several simplifications by the SA-CG method. In particular, 1. the CG error norm for a given iteration is obtained  $d$  iterations latter; 2. each  $j_i^q$  defines one linear system; the sum of the squares of the error norm limits for all  $j_i^q$  is considered as the squared norm of the error of (19); 3. the error norm limit for all combined variables just considers the electrode potentials. The effect of all such approximations is that the algorithm proposed in Section 5.1 overestimates the error at each CG iteration. Simplification 3 is particularly concerning as it scales poorly with mesh density.

To better understand those simplifications, let  $x_i$  be a CG solution of linear system  $Ax = b$  at the  $i$ -th iteration. The error  $L_2$  norm is given by

$$x_i^T A^{-2} x_i - 2b^T A^{-1} x_i + b^T b$$

where  $A^{-2} = (A^T A)^{-1}$ . The evaluation of quadratic form  $x_i^T A^{-2} x_i$  as a byproduct of CG is particularly difficult [63]. Instead, iterative evaluations of quadratic forms such as  $x^T A^{-1} x$  are significantly easier [66].

Martins and Tsuzuki [67], Martins et al. [19] proposed an alternative EIT MAP reconstruction model that uses this property. The idea is to invert the consideration of a perfect FEM and errors in measurements. While motivated by numerical concerns, this approach is justified by the observation that FEM errors may produce even larger errors than measurement noise [68].

By adding an error term in (3) and reordering it so that the electrode nodes are at the final positions of the vectors,

$$\begin{pmatrix} K_{jj} & K_{jc}^T \\ K_{jc} & K_{cc} \end{pmatrix} \begin{pmatrix} \phi_{i,u}^q \\ \phi_{i,m}^q \end{pmatrix} + e = \begin{pmatrix} 0 \\ j_i^q \end{pmatrix} \quad (34)$$

where  $e$  is the *model* error,  $\phi_{i,m}^q$  is the vector of *measured* electric potentials,  $j_i^q$  is the vector of injected currents,  $\phi_{i,u}^q$  is the vector of (unknown) electric potentials inside the domain for a given  $J_i^q$  and  $K_{jj}$ ,  $K_{jc}$  and  $K_{cc}$  are blocks of the matrix  $K$ . Expression (34) can be rearranged as  $\hat{K} \cdot \phi_{i,u}^q + e = \hat{j}_i^q(\phi_{i,m}^q)$  where

$$\hat{K} = \begin{pmatrix} K_{jj} \\ K_{jc} \end{pmatrix} \quad \hat{j}_i^q(\phi_{i,m}^q) = \begin{pmatrix} -K_{jc}^T \cdot \phi_{i,m}^q \\ j_i^q - K_{cc} \cdot \phi_{i,m}^q \end{pmatrix}. \quad (35)$$

Now, for a given  $\phi_{i,u}^q$  and a conductivity distribution  $\sigma$ , the probability of a measure  $\phi_{i,m}^q$  is given by

$$\pi(\phi_{i,m}^q | \phi_{i,u}^q, \sigma) = P(\hat{j}_i^q(\phi_{i,m}^q) - \hat{K}(\sigma) \cdot \phi_{i,u}^q), \quad (36)$$

where  $P(e)$  is the probability density function for the model error  $e$ . Unlike (17), this probability now depends on *two* sets of unknown variables, conductivity distribution  $\sigma$  and the internal electric potentials  $\phi_{i,u}^q$ . If  $\mathcal{J} = \{\phi_{1,u}^q, \dots, \phi_{N,u}^q\}$  is the set of unknown electric potentials for each applied  $j_i^q$ ; then, following the development of (18), one has

$$\pi(\sigma, \mathcal{J} | \mathcal{M}) \propto \pi(\mathcal{J}) \pi(\sigma) \prod_{i=1}^N P(\hat{j}_i^q(\phi_{i,m}^q) - \hat{K}(\sigma) \phi_{i,u}^q). \quad (37)$$

If  $P(e)$  follows a Gaussian independent distribution, then the maximum a posteriori estimation for both conductivity distribution  $\tilde{\sigma}$  and internal potentials  $\tilde{\mathcal{J}}$  is given by:

$$\left( \tilde{\sigma}, \tilde{\mathcal{J}} \right) = \arg \min_{\sigma, \mathcal{J}} \sum_{i=1}^N \left\| \hat{j}_i^q(\phi_{i,m}^q) - \hat{K}(\sigma) \phi_{i,u}^q \right\|^2 + R(\sigma).$$

For a given  $\sigma$  and  $j_i^q$ , this is a least squares problem in  $\phi_{i,u}^q$  given by

$$\min_{\phi} \left\| \hat{j}_i^q - \hat{K}\phi_{i,u}^q \right\|^2 = \hat{j}_i^{qT} \hat{j}_i^q - \hat{j}_i^{qT} \hat{K} (\hat{K}^T \hat{K})^{-1} \hat{K}^T \hat{j}_i^q, \quad (38)$$

as simplification  $\hat{j}_i^q(\phi_{i,m}^q)$  and  $\hat{K}(\sigma)$  are represented as  $\hat{j}_i^q$  and  $\hat{K}$ . The EIT inverse problem is concerned solely with the estimation of  $\sigma$ . As such, the  $\mathcal{I}$  variables can be discarded in (37) and, finally, this is the formulation of a MAP for  $\sigma$

$$\begin{aligned} \tilde{\sigma} &= \arg \min_{\sigma} \sum D_l^2 + R(\sigma) \\ D_l^2 &= \hat{j}_i^{qT} \hat{j}_i^q - \hat{j}_i^{qT} \hat{K} (\hat{K}^T \hat{K})^{-1} \hat{K}^T \hat{j}_i^q \end{aligned} \quad (39)$$

Although the value of  $D_l^2$  in (39) can be fully evaluated using a linear solver, it is shown it can be partially evaluated with increasingly tighter boundaries.

Expression (39) has the quadratic form  $u^T f(A)u$ , where  $u = \hat{j}_i^q$  is a vector,  $A = \hat{K}^T \hat{K}$  is a positive definite matrix and  $f(x) = x^{-1}$  is an analytic function, and it can be efficiently obtained using a connection between the Lanczos Algorithm (LA) and the Gaussian Quadrature (GQ). Martins and Tsuzuki [67], Martins et al. [19] adapted the “Lanczos Bidiagonalization II” to exploit matrices such as  $A = \hat{K}^T \hat{K}$  which are already in the decomposition form to evaluate (39). This is why this algorithm is here called herein SA-LB.

The upper boundary for  $D_l^2$  can be obtained by some algebraic manipulation and a QR factorization. To determine the lower boundary for  $D_l^2$  it is necessary to determine the lowest eigenvalue of  $\hat{K}^T \hat{K}$  [69, chapter 20].

The graph in Fig. 17 compares both SA approaches and shows that the number of iterations required to partially evaluate the objective function using SA-LB is less expensive at later iterations and, for earlier iterations, SA-CG is less expensive. The graph shows outer iterations instead of temperature as the two approaches have distinct temperature scales.

### 5.3. Combining Both SA Approaches (SA-CG and SA-LB)

While much well-suited for iterative evaluation, this new objective function (39) used by SA-LB also has its drawbacks, specifically the required inner iterations for estimating the smallest eigenvalue of  $\hat{K}^T \hat{K}$ .

This requirement impacts the overall algorithm performance, as the number of iterations needed for a good eigenvalue estimation is less than that required for adequate boundaries on the objective function, particularly at the early steps.

Albeit cheaper, reconstruction through SA-LB is more expensive than regular SA-CG in the earlier reconstruction stages. This leads to the idea of performing a two-step reconstruction:

start the reconstruction process using the SA-CG technique, then switch to the SA-LB technique *while keeping the optimization variable state*. If both objective functions have approximately the same convergence trajectory, this should allow a cheaper reconstruction method than both approaches: SA-CG [18, 61, 62] and SA-LB [67, 19]. A possible combination of the methods was proposed by Martins and Tsuzuki [70].

For that, it is necessary to create a common annealing temperature scale between both objective functions. For that, the solution rejection rate  $\times$  temperature for both objective functions is plotted. Fig. 20 shows that it is possible to find a temperature scale for which both curves match reasonably well. The swap point was chosen as the point at which the rejection rate reaches 50%. The performance of the two-steps reconstruction can be seen in Fig. 19. As verified, the objective function swap is performed reasonably well, as the evolution of the SA-LB reconstruction is very similar to that in Fig. 17. The total cost is 22% cheaper than a pure SA-CG reconstruction, and 9% cheaper than a pure SA-LB reconstruction. The generic SA algorithm has two phases: first phase, whereby the domain is explored, and second phase, whereby the solution is detailed. It seems that both methods have characteristics associated to one of the SA phases.

#### 5.4. Markov Chain Monte Carlo Method

MCMC methods are algorithms used to sample from complex distributions such as (18). One of these algorithms is the *Metropolis-Hastings* algorithm [71]. It inspects points from the distribution domain one by one. At each iteration it inspects a *neighborhood* of the currently inspected point  $i$ . A new point  $j$  is elected from this neighborhood with probability  $q(j, i)$ . Finally, a Bernoulli trial is performed with success probability  $\alpha$ . If the trial is successful,  $j$  replaces  $i$  as the current point. Otherwise,  $i$  is kept. Probability  $\alpha$  is given by

$$\alpha = \max\left\{1, \frac{\pi_j q(j, i)}{\pi_i q(i, j)}\right\} \quad (40)$$

where  $\pi_i$  is the desired distribution. By taking a large enough number of iterations, the expected probability of  $i$  is  $\pi_i$ .

The problem with MCMC applied to sample distributions such as (18) is that its evaluation requires the computation of every  $\phi_{i,e}^q(\sigma)$  at each iteration, which requires the solution of  $N$  linear systems *per iteration*. This approach leads to overwhelming computational costs.

Martins et al. [18, 61], Martins and Tsuzuki [62] proposed a *partial* evaluation of  $\phi_{i,e}^q(\sigma)$  by taking error estimates of underlying CG Algorithms used to solve each linear system. A similar approach will be adopted here.

By adopting  $q(j, i) = q(i, j)$  (this is a *symmetric* neighborhood, similar to the one used in [18]). Now, if  $\pi_i$  is defined by (19) and  $E(\sigma)$  is defined as

$$\sum_{i,j=1}^N \left\| \phi_{i,m}^q[j] - \phi_{i,e}^q(\sigma)[j] \right\|^2 + \gamma^2 R(\sigma)$$

and the probability  $\alpha$  in (40) is taken as,

$$\alpha = \max \left\{ 1, e^{(E(i) - E(j))/\gamma^2} \right\} \quad (41)$$

or, by writing  $E_{j,i} = E(i) - E(j)$ , and  $\alpha = \max \{1, e^{-E_{j,i}/\gamma^2}\}$ , then  $\pi_i = \pi(i|\mathcal{M})$ . The values  $E(i)$  and  $E(j)$  can be estimated with a *bounded* error by a *partial* execution of CG algorithms for each current injection pattern [18].

Let  $\Delta\tilde{E}_{j,i}$  be the estimated variation of  $E$  between points  $i$  and  $j$ ,  $\Delta\bar{E}_{j,i}$ ,  $\Delta\underline{E}_{j,i}$  its upper and lower boundaries respectively. Let  $\beta \ll 1$  a constant. Then if

$$e^{-\Delta\bar{E}_{j,i}/\gamma^2} \geq \begin{cases} 1 - \beta & \text{if } \Delta\tilde{E}_{j,i} \leq 0, \\ e^{-\Delta\underline{E}_{j,i}/\gamma^2} - \beta & \text{if } \Delta\tilde{E}_{j,i} > 0 \end{cases} \quad (42)$$

$$e^{-\Delta\underline{E}_{j,i}/\gamma^2} \leq \min \left\{ 1, \beta + e^{-\Delta\bar{E}_{j,i}/\gamma^2} \right\} \quad (43)$$

then, as  $\beta$  approaches 0,  $\pi_i$  is a distribution within the *bounded* distance of the desired distribution in (19). This is a special case of a *Noisy Metropolis Hasting Algorithm*, as described in [72].

As seen in [18, 61, 62], even for very small values of  $\beta$  (around 0,5%), boundaries from (31,32) can be reached by a fraction of CG iterations that would usually be required.

Martins and Tsuzuki [73] implemented a MCMC algorithm for absolute EIT with incomplete objective function evaluation. Data from the experiment performed in [18, 19] with cucumber slices disposed on a saline solution in a prismatic fashion, provided a 2D Phantom. The same “Gradient Norm” Regularization as in [18, 19] was used here. The final distribution average value and standard deviation (Square Root of each component self-correlation) are 545 depicted in Fig. 21.

## 5.5. Gauss-Newton Method

The G-N method is often used to solve non-linear least square problems to minimize functions  $F_0$  of the form

$$F_0(x) = \frac{1}{2} \|e(x)\|_2^2 = \frac{1}{2} e(x)^T e(x), \quad (44)$$

where  $x$  is a real  $n$ -vector  $x = (a_1, a_2, \dots, a_n)^T$  and  $e(x) = (e_1(x), e_2(x), \dots, e_m(x))^T$  is a function  $e: \mathbb{R}^n \rightarrow \mathbb{R}^m$ .

In this method, the Hessian of function  $F_0$  is approximated by  $\nabla^2 F_0(x) \approx J(x)^T J(x)$  and the iteration of the G-N method can be computed as

$$x_{k+1} = x_k + \alpha_k \Delta x_k, \quad (45)$$

$$\Delta x_k = (J(x_k)^T J(x_k))^{-1} (J(x_k)^T F_0(x_k)), \quad (46)$$

where  $J(x_k) \in \mathbb{R}^{n \times m}$  is the Jacobian matrix of  $F_0(x_k)$  and  $\alpha_k$  is the step size of iteration  $k$ .

The approximation of the Hessian matrix is valid when the initial guess is close to the minimum of the function. For more details about the convergence of the method, the matrices computation and the effectiveness of Newton's methods can be found in references [74, 75].

If we have an observation model of the form

$$\phi_m^q = \phi_e^q(\rho) + e(\rho), \quad (47)$$

where  $\rho \in \mathbb{R}^n$  is a vector of resistivity and  $n$  the number of resistivity regions to be determined, the eq. (44) can be rewritten as

$$\begin{aligned} F_0(\rho) &= \frac{1}{2} e(\rho)^T e(\rho) \\ &= \frac{1}{2} (\phi_m^q - \phi_e^q(\rho))^T (\phi_m^q - \phi_e^q(\rho)). \end{aligned} \quad (48)$$

Due to the ill-posed nature of the EIT problem, the least square method shown in the eq. (48) needs to be regularized. Using the generalized Tikhonov regularization theory [75], a new term is added,

$$\begin{aligned} F_1(\rho) &= \frac{1}{2} (\phi_m^q - \phi_e^q(\rho))^T (\phi_m^q - \phi_e^q(\rho)) + \\ &\quad \lambda^2 (\rho - \rho^*)^T L^T L (\rho - \rho^*), \end{aligned} \quad (49)$$

where  $L$  is called regularization matrix,  $\rho^*$  is the initial guess and  $\lambda$  is the regularization parameter.

Several kinds of regularization can be used in EIT. The non-negativeness of the resistivity is used to restrict the solution space [76]. Smoothing filters [77] (e.g. Gaussian low pass filters) are also used when the resistivity distribution is known to be smooth. Minimal total variation may be used when the resistivity distribution is known to have sharp variation in space [78].

Another possibility is the use of statistical priors [23, 28] to build the regularization term of the problem. For thorax applications an anatomical and physiological atlas can be computed using segmented tomographic images and measured resistivities of the thorax tissues.

**5.5.1. The Use of Anatomical Atlas for Thorax Application**—An anatomy-based prior for biomedical applications of EIT was reported and the benefits are shown through a

numerical example [79]. Based on this approach, images of swine thorax are estimated by the G-N method to validate the use of anatomical atlas for absolute images.

Assuming that the probability density function (PDF) of the resistivity distribution in the swine thorax,  $\pi(\rho_{sw})$ , can be described as a Gaussian distribution,

$$\pi(\rho_{sw}) \propto e^{-\frac{1}{2}(\rho - \bar{\rho}_{sw})^T \Gamma_{sw}^{-1} (\rho - \bar{\rho}_{sw})}, \quad (50)$$

the mean ( $\bar{\rho}_{sw}$ ) and covariance matrix ( $\Gamma_{sw}$ ) of the PDF can be used to estimate the swine thorax images. The prior information is the regularization term (second term) of equation 49,

$$\begin{aligned} F_2(\rho) = & \frac{1}{2}(\phi_m^q - \phi_e^q(\rho))^T (\phi_m^q - \phi_e^q(\rho)) + \\ & \gamma^2(\rho - \bar{\rho}_{sw})^T \Gamma_{sw}^{-1} (\rho - \bar{\rho}_{sw}) + \\ & \lambda^2(\rho - \bar{\rho}_{sw})^T F^T F (\rho - \bar{\rho}_{sw}) \end{aligned} \quad (51)$$

where  $F$  is an Gaussian high pass filter,  $\Gamma_{sw}$  is the covariance matrix of the statistical prior, interpolated to the FEM mesh,  $\bar{\rho}_{sw}$  is the expected vector of resistivities of the statistical prior also interpolated to the FEM mesh,  $\gamma$  is the regularization parameter for the prior information. The third term is not necessary if the prior information is informative enough in all the directions in which the first term is not informative.

In eq. (51) the first term comes from the likelihood, the second term is the prior information and the third term is a smoothness prior. It penalizes spatial high frequency image components of the difference between candidate  $\rho$  and the statistically expected  $\bar{\rho}_{sw}$ .

**5.5.2. Anatomical Atlas Computation**—According to Kaipio and Somersalo [23] the construction of the prior information may be the most challenging part of the solution of an inverse problem. Most of the swine chest tissues impeditivity data present in the literature were measured *in vitro* [80] and do not reflect the variations caused by ventilation or perfusion. Those variations must be considered and *in vivo* measurements of the resistivity of the tissues are required. The resistivity distribution (mean and variance) of each tissue was obtained from the literature [80] and from *in vivo* experiments [81].

To estimate the anatomical atlas, expected value and covariance matrix,  $\pi(\rho_{sw})$ , a set of 39 CT scans of swine chests from 25 different animals were taken as tomographic samples to compute the anatomical atlas. For each CT scan, 5 images at different levels were used (center,  $\pm 20\text{mm}$  and  $\pm 40\text{mm}$ ), generating a 3-dimensional image.

Five different tissues – bones, aerated lungs, atelectasis, heart and muscles – were identified according to their characteristics concerning grey levels. This task was achieved by an image processing algorithm comprising: 1) a manual thresholding operation, to separate different grey level regions; 2) a chain of morphological operators, to eliminate undesirable artifacts and to smooth the boundaries of the remaining ones.

The anatomical atlas requires an ensemble of 2D resistivity images generated from segmented tomographic CT scan images and the resistivity distribution of each segmented tissue. A Gaussian distribution of resistivity was assigned to each segmented tissue of the tomographic images. The expected values vector and the covariance matrix of the anatomical atlas were computed. The resistivity distribution of each tissue was considered Gaussian and was obtained from the literature [80] or measured from *in vivo* experiments [81].

**5.5.3. In vivo Images**—Clinical emergencies were sequentially induced on the lungs of a swine specimen, atelectasis, pleural effusion and pneumothorax. Electrical impedance tomography images and CT scans were collected *in vivo*.

The Finite Element Mesh used was created with real shape and electrode position obtained from the CT images. The Approximation Error Theory was used to reduce discretization effects and mesh size errors in the forward problem. Then, the resistivity images were estimated minimizing  $F_2(\rho)$  by using the G-N method.

Figure 22 presents the mean of the resistivity distribution  $\bar{\rho}_{sw}$  at 5 different levels. An additional color scale is plotted since the mean resistivity of the bone tissue is much higher than the others tissues.

Figure 23 presents both CT scans and resistivity images obtained at 5 different levels, while the animal was being ventilated with a positive end-expiratory pressura (PEEP) of 5  $cmH_2O$ . Atelectasis can be observed on the posterior side of the lungs in the CT image. The resistivity image shows a low resistivity area in the same region, as expected.

Later, the ventilation pressure was increased to a PEEP of 25  $cmH_2O$  (see Fig. 24). The resistivity image presents higher values of resistivity for both lungs. The ventilation pressure was then reduced to a PEEP of 12  $cmH_2O$  and pleural effusion was artificially induced by injecting a  $NaCl$  saline solution of 0.9%. Fig. 25 shows the CT scans and resistivity images obtained. The area where the pleural effusion occurred shows lower resistivity in the EIT image.

A low resistivity area near the spinal cord appears at all resistivity images. This may be caused by the aorta (marked as light red in the CT images to help comparison), as the blood is highly conductive. Note that the aorta was not considered in this anatomical atlas.

The results show that image reconstruction of swines is feasible when the anatomical atlas and a smoothness regularization term are used together. The number of CT scans available was small, 39; the co-variance matrix and expected distribution of resistivity should thus not be considered of high statistical quality. Even with this small number of CT scans, the anatomy based prior seems to be able to serve for regularizing the EIT inverse problem. The atelectasis and the pleural effusion are present in the EIT images. The present analysis is qualitative, and a quantitative study is in progress.

## 5.6. Bayesian Filtering: Unscented Kalman Filters

EIT depends on electric potentials and currents measurements on the electrodes to estimate the electrical impeditivity distribution often using a finite element mesh as described previously. However, the FEM mesh is very often imprecise in many respects, e.g., precise electrode position, electrode spacing, electrode size, shape of the region under study and required FEM discretization level. Also, data collection is subject to external interference.

The Bayesian approach deals with problems whereby a level of uncertainty in the models is present and cannot be disregarded. The goal of the Bayesian inversion is to extract information about the unknowns and to determine the level of uncertainty based on all available measured data and prior models.

When the system under observation contains dynamic characteristics, adding *prior* information to the estimation problem is desirable as an evolution model. For this, Bayesian filtering is a feasible choice.

The problem is now to estimate the state over time  $\sigma_0^K = \{\sigma_0, \sigma_1, \dots, \sigma_K\}$  using the set of collected measurements  $\phi_1^K = \{\phi_1^q, \phi_2^q, \dots, \phi_K^q\}$  acquired at equal spaced time instants,  $t_k = kT_s$ ,  $k = 1, 2, \dots$  from the observation model (16)

Let the following equations denote the evolution and observation models of the region under EIT monitoring

$$\sigma_{k+1} = \Phi_k \sigma_k + v_k, \quad (52)$$

$$\phi_k = J_k \sigma_k + w_k. \quad (53)$$

where  $\Phi_k$  is the transition matrix of the system,  $J_k$  is the linearized Jacobian of the observation model,  $v_k$  and  $w_k$  are process and observation noise and  $h(\sigma)$  is the FEM solution of the forward problem. It can be shown [23] that the Bayesian filtering problems can be divided into two steps. The *propagation step* is responsible for advancing the probability distribution over time between the instant  $t_k$  and  $t_{k+1}$  when a new measurement is available.

$$\pi_{\sigma_{k+1} | \phi_1^k} = \int \pi_{\sigma_{k+1} | \sigma_k} \times \pi_{\sigma_k | \phi_1^k} d\sigma_k. \quad (54)$$

The *update step* is responsible for incorporating the new measurement to the estimate of  $\sigma_{k+1}$ .

$$\pi_{\sigma_{k+1} | \phi_1^{k+1}} = \frac{\pi_{\phi_{k+1} | \sigma_{k+1}} \times \pi_{\sigma_{k+1} | \phi_1^k}}{\pi_{\phi_{k+1} | \phi_1^k}}. \quad (55)$$

Under Gaussian assumptions, these integrals can be computed analytically, obtaining the set of equations of the UKF.

$$\pi_{\sigma_{k+1}|\phi_1^k} \propto \exp \left( -\frac{1}{2} \left\| \phi_{k+1} - H_{k+1} \sigma_{k+1} - \bar{v}_k \right\|_{(\Gamma_{k+1}^{vv})^{-1}}^2 \right. \\ \left. - \frac{1}{2} \left\| \sigma_{k+1} - \Phi_k \bar{\sigma}_k - \bar{w}_k \right\|_{(\Gamma_{k+1|k}^{\sigma\sigma})^{-1}}^2 \right), \quad (56)$$

where  $\|x\|_A^2 = x^T A x$  and  $\Gamma_{k+1|k}^{\sigma\sigma} = \Phi_k \Gamma_k^{\sigma\sigma} \Phi_k^T + \Gamma_{k+1}^{ww}$ .

Additional Gaussian *prior* information can be included by multiplying (56) by terms similar to

$$\pi_{\sigma}^{prior} \propto \exp \left( -\frac{\alpha^2}{2} \|L_r(\sigma - \sigma^*)\|_2^2 \right) \quad (57)$$

$$\Gamma^{\sigma\sigma} = \frac{1}{\alpha^2} (L_r^T L_r)^{-1}. \quad (58)$$

Gaussian distributions can generate a large class of *prior* information due to their formulation, ease of analytic treatment and versatility [23].

The classic (linear) UKF and its nonlinear variations have been implemented for EIT applications in several situations [82, 83, 84, 85, 86, 87, 12, 88, 89, 90]

**5.6.1. Dual Estimation with Unscented Kalman Filter**—In cases in which the evolution model has a set of parameters  $p$  to be adjusted, as usual in medical applications, Kalman filters can also be used. At first,  $\sigma_k$  and  $p_k$  should be jointly estimated. For this, one must create an augmented state composed of these two vectors, to compose new evolution and observation models with the original models, and to determine  $\pi_{\sigma_k, p_k | \phi_k}$ . This method is often called *joint estimation*. However, the required computational load can be prohibitive in real time prediction or filtering.

One way to deal with this challenge is to use an alternative method, first proposed in [91] for a bilinear system. This method, called *dual estimation*, consists of using two Kalman filters running in parallel, one for estimating  $\sigma_k$  and the other for  $p_k$ . In this approach, the most current estimate of one filter is used in the other as a fixed parameter, thus, determining  $\pi_{\sigma_{k+1}|p_k, \phi_1^k}$  and  $\pi_{p_{k+1}|\sigma_k, \phi_1^k}$ . This method ignores possible correlations between

these vectors and is, therefore, an approximation. The diagram in Fig. 26 shows the implementation of these two filters in parallel.

**5.6.2. Dynamic Prior of the Ventilation Mechanics**—During respiration, the lungs are influenced by the pressure of the pleural space, by the resistance of the air flow in the airways of gravitation, by gravitational effects on its structure, by the elasticity of the lung

tissue, and by effects of the surface tension of the lubricant covering the alveoli. The inertial effects of the pulmonary tissues are generally negligible in comparison with the resistive and elastic effects.

Volume increases must overcome increasing resistances to expansion. This is caused by the stiffness of the thoracic cage and also by physical limitations of lung tissue. Close to the minimum volume, inter-pleural cavity pressure starts to limit further reductions in volume. This relationship is known as Volume-Pressure relation, which can be successfully modeled by a sigmoidal function [92].

$$V = a + b \left[ 1 + \exp\left(-\frac{P - e}{d}\right) \right]^{-1}, \quad (59)$$

where  $a, b, c, d$  are adjustable parameters and are associated with different illnesses.

Several models for the pulmonary mechanics can be found in the literature [93, 94, 95, 96, 97, 92]. A multicompartmental nonlinear model of the lungs under ventilation can be created.

The model is composed of  $N_c$  compartments, excited by the pressure of the upper respiratory tract and features elastic and viscous behavior. The model can be seen in Fig. 27. Effective pressure  $P(t)$  excites each of the compartments to increase their volumes  $V_i(t)$ . Elastic restitution with stiffness  $K_i(V_i)$ , which is a function of air volume and viscous resistance  $c_i \dot{V}_i$ , is also present.

The volume within each compartment is given by

$$\dot{V}_i(t) = \frac{P(t)}{c_i} - \frac{1}{2c_i} \frac{\partial V_i}{\partial K_i} V_i^2 - \frac{K_i \cdot V_i}{c_i}. \quad (60)$$

where the stiffness  $K_i(V_i)$  can be obtained from (59)

$$K = \frac{\partial V}{\partial P} = \frac{bd}{(V-a)[b-(V-a)]}, \quad V \in ]a, a+b[ \quad (61)$$

At each time instant  $t_k$ , it is possible to integrate (60) between  $t_k$  and  $t_k + \Delta t$  and find  $V_i(t_k + \Delta t)$ .

$$V_i(t_k + \Delta t) = V_i(t_k) + \int_{t_k}^{t_k + \Delta t} \dot{V}_i(t) dt, \quad i = 1, \dots, N_c. \quad (62)$$

This function can be used as a dynamic prior of the lungs after converting these values to average conductivities in each compartment [98].

The number of compartments must be chosen to balance the simplicity of the parameter estimation step with sophistication to improve the prediction step of the Kalman filter. With a greatly simplified model, consisting of only one compartment, it is possible to describe a

pair of lungs well under very similar physiological conditions. However, it would not be possible to model localized abnormalities such as differences in lung capacity or pneumothoraxes. In a model with left/right compartments, differences between the lungs is allowed but it is still not possible to model, as one example, variations by gravitational effects. Moura et al. [89] showed that only a small number of modes could be enough to be used in the Kalman filter.

**5.6.3. Experimental Results**—Dual estimation with the UKF was used to estimate state  $\rho = \sigma^{-1}$  in parallel with the parameters of the evolution model of the lungs composed of two compartments (L/R). An automatic image segmentation step identifies the compartments of the lungs and selecting the appropriate evolution model [99]. Image segmentation is performed in the estimated distribution of resistivity  $\rho$ .

Figure 28 presents the average resistivity value estimated by UKF in each compartment (L/R) of the lung of a non-smoking male subject. The estimated average resistivity stays between 6 and 7  $\Omega \cdot m$  in both lungs during the experiment. The estimates oscillated more during the two first cycles until the state and the segmentations were properly adjusted. After this initial period, temporal variations become more regular. The figure also presents two images at peak inspiration and expiration and the segmented compartments.

## 5.7. D-Bar

The D-bar method is a direct (non-iterative) solution method for the inverse conductivity problem, and these methods originate in mathematical uniqueness proofs, beginning with Calderón's proof that the linearized problem in dimension  $n = 2$  is injective [100]. He also proposed a direct reconstruction method for approximating conductivities that are a small perturbation from a constant. The reader is referred to [101] for a review of these proofs, which address various smoothness assumptions about the conductivity, the reconstruction of complex-valued conductivities, reconstructions from partial boundary data, and 2-D versus 3-D reconstructions.

The D-bar approach for reconstructing PDE coefficients from boundary measurements was first formally suggested by Novikov [102] for  $n = 2$  in 1987, and rigorously analyzed by Nachman [103] in 1988 ( $n = 3$ ) and 1996 ( $n = 2$ ) [60]. In this section we focus on the 2-D D-bar method based on Nachman's 1996 uniqueness proof [60]. We chose to focus on this D-bar method since it is arguably the most developed of the direct EIT reconstruction algorithms. The first numerical inversion method based on [60] was published in 2000 by Siltanen et al. [59]. The method was later successfully applied to real data [104, 105] and shown in 2009 to provide a formal regularization strategy for the highly nonlinear inverse problem of EIT [106]. The regularization is accomplished via low-pass filtering in the scattering transform with a cutoff frequency dependent upon the noise level. The effect of domain-shape modeling and measurement errors on the 2-D D-bar method was analyzed in [107], and the method was used in the analysis of clinical data in [108, 109].

The data for D-bar methods is formulated in terms of the DN, or voltage-to-current density map defined by

$$\Lambda_\gamma(u|_{\partial\Omega}) = \gamma \frac{\partial u}{\partial \nu} \Big|_{\partial\Omega}. \quad (63)$$

The linear operator  $\Lambda_\gamma$  is a mathematical model for the set of all infinite-precision electric boundary measurements.

A commonality of D-bar methods is the use of *complex geometrical optics* (CGO) solutions to a related PDE, which differs from method-to-method. These CGO solutions are important once they grow exponentially in some directions, and decay exponentially in others.

Calderón's method introduced the CGO solutions

$$u_1(z) = e^{i\pi(\xi \cdot z) + \pi(a \cdot z)} \quad (64)$$

$$u_2(z) = e^{i\pi(\xi \cdot z) - \pi(a \cdot z)}, \quad (65)$$

where  $a, \xi \in \mathbb{R}^2$  with  $\xi \cdot a = 0$  and  $|\xi| = |a|$ , to Laplace's equation for the linearized inversion method. Three-dimensional EIT algorithms based on CGO solutions were discussed and implemented in [110, 111, 112, 113, 114, 115]. In the D-bar method presented here, the CGO solutions are special solutions to the Schrödinger equation involving an artificial complex frequency variable  $k$ , and they are the key to the direct computation of the conductivity. As seen further on, the CGO solutions can be directly computed from the measured data.

The general outline of the D-bar method is as follows:

1. Compute a finite-dimensional approximation to the DN map  $\Lambda_\sigma$  from the measured data.
2. Compute an approximation to the CGO solution  $\psi$  on the boundary of the domain.
3. Compute an approximation to the nonlinear Fourier transform, known as the scattering transform.
4. Solve the D-bar equation numerically on a finite grid determined by the cutoff frequency.
5. Determine the conductivity by evaluating the solution of the D-bar equation at frequency  $k = 0$ .

The first step in a practical implementation of the D-bar method is to compute a finite-dimensional approximation to the DN map. This is discussed in Section 5.7.1. We then provide the mathematical equations of the D-bar method in Section 5.7.2 and refer the reader to [101] for their numerical solution. Absolute images from experimental data are included in Section 5.7.4.

**5.7.1. Formation of the DN Map from Measured Data**—The direct reconstruction methods in this chapter all require a matrix approximation to the DN map; that is, a matrix

that approximates the action of the DN map in any given voltage pattern. The dimension of the approximation depends on the number of linearly independent current patterns being applied. For example, for  $L$  electrodes, the trigonometric current patterns result in  $L-1$  linearly independent patterns, and the DN matrix will be of size  $L-1$  by  $L-1$ . Bipolar injection patterns that skip  $\alpha$  electrodes between the injection electrodes result in  $L - \gcd(L, \alpha + 1)$  linearly independent patterns. Let the basis of orthonormal current patterns be denoted by  $\phi^n$ , where  $n = 1, \dots, N$ ,  $N < L$ , and denote the vector of voltages on the electrodes arising from the  $n$ -th current pattern by  $U^n$ .

Denoting the DN matrix by  $\mathbf{L}_\sigma$ , we have that  $\mathbf{L}_\sigma$  is the inverse of the matrix approximation  $\mathbf{R}_\sigma$  to the Neumann-to-Dirichlet map, provided that the voltage measurements sum to zero for each current pattern. Since the usual data collection scenario is to apply current and measure voltage, one can form  $\mathbf{R}_\sigma$  from the discrete inner product, and invert the matrix to obtain  $\mathbf{L}_\sigma$ . As long as the matrix of current patterns is full rank,  $\mathbf{R}_\sigma$  will be a well-conditioned matrix. Thus, setting

$$\mathbf{R}_\sigma(m, n) = (s_\ell \phi^m, U^n)_L, \quad (66)$$

where  $s_\ell$  is the arc length of the boundary segment connecting the centers of electrodes  $\ell$  and  $\ell + 1$ , we have

$$\mathbf{L}_\sigma = \mathbf{R}_\sigma^{-1}. \quad (67)$$

**5.7.2. Equations of the D-bar Method**—The method begins with a transformation of the generalized Laplace equation with a twice differentiable conductivity  $\sigma$  to the Schrödinger equation through the change of variables  $q(z) = \Delta\sqrt{\sigma(z)}/\sqrt{\sigma(z)}$  and  $\tilde{u}(z) = \sqrt{\sigma(z)}u(z)$ , where the point  $z = (x, y)$  lies in  $\Omega$ , a bounded, simply connected Lipschitz domain in  $\mathbb{R}^2$ . This results in

$$-\Delta\tilde{u} + q(z)\tilde{u} = 0, \quad z \in \Omega. \quad (68)$$

Under the assumption that  $\sigma$  is constant in a neighborhood of the boundary of  $\Omega$ , one can extend (68) to the whole plane, taking  $q = 0$  outside  $\Omega$ . In this section, we will assume without loss of generality  $\sigma \equiv 1$  in a neighborhood of the boundary.

To define the CGO solutions, it is necessary to introduce a complex parameter  $k = k_1 + ik_2$  in eq. (68) and require the solution in the plane, which we will denote by  $\psi(z, k)$ , to have asymptotic behavior  $\psi(z, k) \sim e^{ikz}$  for large  $|z|$  or large  $|k|$ , where the spatial variable  $(x, y)$  has been identified with a point  $z$  in the complex plane. The precise formulation of this asymptotic behavior is given below in (70), where  $W^{1,p}(\mathbb{R}^2)$  is the Sobolev space of functions with one weak derivative in  $L^p$  (see, for example, [116]). The CGO solution  $\psi(z, k)$  then satisfies [60]

$$-\Delta\psi(z, k) + q(z)\psi(z, k) = 0, \quad z \in \mathbb{R}^2 \quad (69)$$

$$e^{-ikz}\psi(z, k) - 1 \in W^{1,p}(\mathbb{R}^2), \quad p > 2. \quad (70)$$

There is a CGO solution closely related to  $\psi$  denoted by  $\mu(z, k)$ , where

$$\mu(z, k) \equiv e^{-ikz}\psi(z, k).$$

These solutions are the keys to the reconstruction since the conductivity can be obtained directly from  $\mu$  or  $\psi$  through formula [60]

$$\sigma(z) = \mu^2(z, 0), \quad z \in \Omega. \quad (71)$$

Thus, the idea is to compute the CGO solutions on a grid of points in  $\Omega$ , and compute  $\sigma$  by (71). This strategy depends on a connection between the measured data and the CGO solutions, which is provided by the nonlinear Fourier transform known as the scattering transform  $\mathbf{t}(k)$  and the D-bar equation for  $\mu$ . The scattering transform is defined by

$$\mathbf{t}(k) = \int_{\Omega} e^{ik\bar{z}} q(z) \psi(z, k) dz, \quad (72)$$

and can be regarded as a nonlinear Fourier transform of  $q$  due to the asymptotic behavior of  $\psi$ . It is related to the DN data through an equation that requires knowledge of  $\psi$  on the boundary of  $\Omega$ :

$$\mathbf{t}(k) = \int_{\partial\Omega} e^{ik\bar{z}} (\Lambda_{\sigma} - \Lambda_1) \psi(z, k) ds. \quad (73)$$

Here  $\Lambda_1$  denotes the DN map corresponding to the homogeneous conductivity distribution  $\sigma \equiv 1$ .

To obtain the values of  $\psi$  on the boundary of  $\Omega$ , one can solve the boundary integral equation [60]

$$\psi(z, k)|_{\partial\Omega} = e^{ikz}|_{\partial\Omega} - \int_{\mathbb{R}^2} G_k(z - \zeta) (\Lambda_{\gamma} - \Lambda_1) \psi(\cdot, k)|_{\partial\Omega}, \quad (74)$$

where  $G_k$  is a special Green's function for the Laplacian known as the *Faddeev Green's function* [117] given by

$$G_k(z) = e^{ikz} \int_{\mathbb{R}^2} \frac{e^{iz \cdot \xi}}{\xi(\xi + 2k)} d\xi, \quad -\Delta G_k(z) = \delta(z).$$

The reader is referred to [118, 60, 101] for properties of the Faddeev Green's function  $G_k$ .

The D-bar equation is a PDE with respect to the conjugate of the complex parameter  $k$ . Since  $\frac{\partial}{\partial k}$  is often denoted as  $\bar{\partial}_k$ , and is called a  $\bar{\partial}$  (D-bar) operator; this is the origin of the method name. The D-bar equation satisfied by  $\mu$  is

$$\frac{\partial \mu}{\partial k} = \frac{\mathbf{t}(k)}{4\pi k} e_{-z}(k) \overline{\mu(z, k)}, \quad (75)$$

where  $e_z(k) \equiv e^{i(kz + \bar{k}\bar{z})}$ . Due to the large  $|k|$  asymptotes of  $\mu$  ( $\mu \sim 1$ ), and the generalized Cauchy integral formula, eq. (75) can also be written in integral form as

$$\mu(z, s) = 1 + \frac{1}{(2\pi)^2} \int_{\mathbb{R}^2} \frac{\mathbf{t}(k)}{(s - k)\bar{k}} e_{-z}(k) \overline{\mu(z, k)} dk_1 dk_2. \quad (76)$$

The integral form is used for numerically solving the D-bar equation, and  $\sigma$  is subsequently computed from (71). Alternatively, the D-bar eq. (75) can be solved by a finite-difference method [119].

There are several important observations to be made about the method related to the numerical solution of the equations. First, note that eq. (76) can be solved independently for each value of  $z$  in  $\Omega$ . This facilitates trivial parallelization and the computation of  $\sigma$  in a region of interest. A real-time implementation of the D-bar method is given in [24], where several parallelization strategies are studied. Second, the integral in eq. (76) is over the entire complex plane, and must be truncated for numerical computing. The low-pass filtering of the scattering transform reduces the support (region of nonzero values) of  $\mathbf{t}(k)$  to a bounded region in the  $k$  plane.

In summary, the full nonlinear method is to solve the boundary integral equation for  $\psi$  (74) numerically, compute the scattering transform using (73), solve the D-bar eq. (76), and compute  $\sigma$  from (71).

**5.7.3. Simplifying Assumptions**—The scattering transform requires knowledge of the CGO solution  $\psi$  on the boundary of the domain. However, there are two simplifications of the method that reduce the computational cost. The first is to make what is known as the  $\mathbf{t}^{\text{exp}}$  approximation. In this approach, function  $\psi$  is approximated by its first-order behavior,  $e^{ikz}$  and this approximation is used in the computation of the scattering transform, and defined as  $\mathbf{t}^{\text{exp}}$ :

$$\mathbf{t}^{\text{exp}}(k) = \int_{\partial\Omega} e^{i\bar{k}\bar{z}} (\Lambda_\sigma - \Lambda_1) e^{ikz} ds. \quad (77)$$

This approximation is best suited for low-contrast  $\sigma$ , see, for example [120] for a study on the effect of varying the contrast and support of  $\sigma$  in the reconstruction, but the  $\mathbf{t}^{\text{exp}}$  approximation has proven to be robust for experimental data, including reconstructions of ventilation and perfusion in the human chest [105].

A second-order approximation to  $\psi|_{\Omega}$  and the scattering transform can be computed by taking a first order approximation to Faddeev Green's function in (74). Faddeev Green's function is of the form  $G_k(z) = G_0(z) + H_k(z)$  where  $G_0$  is the standard Green's function for the Laplacian

$$G_0(z) := -\frac{1}{2\pi} \log|z|, \quad (78)$$

and  $H_k(z)$  is the remainder term, a smooth harmonic function of  $z$ . Denoting the resulting approximation to  $\psi$  by  $\psi_0$ , the boundary integral equation for  $\psi_0$  is

$$\psi_0(z, k) = e^{ikz} - \int_{\partial\Omega} G_0(z - \zeta)(\Lambda_\sigma - \Lambda_1)\psi_0(\zeta, k)d\zeta, \quad z \in \partial\Omega. \quad (79)$$

This approach was used to compute reconstructions of perfusion in a 2-D cross section of the human chest in [121].

The  $\psi_0$  and the fully nonlinear approach require the numerical solution of the boundary integral equation. Details of the numerical solutions of the equations can be found in [101] and the references therein.

**5.7.4. Examples of Reconstructions**—Experimental data were collected on a chest-shaped tank with 32 electrodes of width 2.54 cm and 103 cm perimeter filled with conductive saline and targets using the ACE1 pairwise current injection system [122]. Skip-0 current patterns were applied at 125 kHz with a current amplitude of 3 mA. The phantom heart was made of agar measuring 0.26 mS/m using an Omega CDH221 conductivimeter. The phantom lungs were made of watermelon and measured approximately 0.14 mS/m, and the saline measured 0.125 mS/m. We remark that these values are approximate since the conductivimeter operates at 1 kHz. A photo of the experimental configuration is found in Fig. 29a. Absolute images using the D-bar method with the  $t^{\exp}$  approximation to the scattering transform are found in Fig. 29. The method was implemented with a non-uniform truncation radius to control the blow-up of the scattering transform that occurs in the presence of noise. The heart is not visible in the images, but its presence does seem to affect the images by distorting the lungs as the truncation radius  $R$  of the scattering transform increases. This data set was also used in [122], where similar effects were observed in G-N reconstructions, Calderón’s method, and the D-bar method for complex conductivities [123].

Resolution can be improved by incorporating priors in the D-bar method. A method was introduced in [124] in which the scattering transform is augmented outside its original truncation radius, which we call  $R_1$ , by the scattering transform computed from its definition (72) from a spatial prior on a wider radius, which we call  $R_2$ . The larger the  $R_2$ , the stronger the influence of the prior. In addition, the CGO solution  $\mu(z, k)$  computed directly from the prior by definition can be included in the integral form of the D-bar eq. (76), and its influence is controlled through a weighting parameter  $0 < \alpha < 1$ , with smaller  $\alpha$  implying more influence of the prior on the reconstruction. The reader is referred to [124] for a thorough explanation of this method of including priors in D-bar. The method was extended to use optimization in choosing conductivity values for the prior [125], as well as for problems with partial boundary data [126], the D-bar method for complex conductivities [25], and dynamic priors for human data [127].

Spatial priors for the data used here were created by defining organ shapes from the photo and assigning conductivity values corresponding to the values measured by the conductivimeter to each organ region. Results using the method in [124] with several values of  $R_1$ ,  $R_2$ , and  $\alpha$  are shown in Fig. 30. Even the weak priors in Figs. 30a and 30b significantly improve the resolution of the image, and reveal the heart. The moderate prior in Fig. 30c yields well-resolved lungs and heart.

**5.7.5. For Further Reading**—In [128], the effects of errors in the domain shape and electrode placement on absolute images computed with 2-D D-bar reconstruction algorithms are studied in experimental data. This work includes the D-bar method for reconstructing complex-valued conductivities introduced in [129, 130], based on the theoretical proof of unique determination in [131] and with the algorithm developed in [123]. This method relies on the solution of an elliptic system of D-bar equations, as in proof [132] for the real-valued case. Also see [133] for absolute images of complex-valued conductivities. Calderón’s method is another source of absolute images, and can be viewed as a linearization of the D-bar method [134]. See [135, 119, 136, 122] for implementation details and absolute and difference images with Calderón’s method.

## 5.8. Multiple-Objective Approach

Regularization of inverse problems posed as optimization processes often appears as new terms in MOSA objective function. The determination of the appropriate weight for those terms is a difficult problem in itself.

An alternate approach is to consider both the function in (19) and regularization terms as concurrent objective functions to be minimized. In this case, there is no single solution that satisfies all objectives simultaneously [137]. This optimization category is called “multi-objective optimization”. Multi-objective optimization problems do not admit a single solution, having instead a set of mutually non-dominating solutions. In a minimization problem, a solution  $x_i$  is said to dominate  $x_j$  if  $\forall k \in 1, 2, \dots, M$ ,  $f_k(x_i) \leq f_k(x_j)$  and  $\exists k \in 1, 2, \dots, M$ , such that  $f_k(x_i) < f_k(x_j)$  [138]. Thus, if  $x_i$  dominates  $x_j$ ,  $F(x_i)$  is at least as good as  $F(x_j)$  for all objectives, and that there is at least one objective for which  $F(x_i)$  is strictly better than  $F(x_j)$  [139]. A solution  $\vec{y}$  is considered Pareto optimal if and only if there is no other solution that dominates it. The set of Pareto optimal solutions is called the Pareto optimal set [139]. Fig. 31 shows a representation of the Pareto front in a bi-objective problem in which we want to minimize  $f_1$  and  $f_2$ .

Martins et al. [140] adapted the algorithm Multi-Objective Simulated Annealing (MOSA) developed by Engrand [141] to find the Pareto front for the multi-objective problem of simultaneously minimize both equations in (19). Martins and Tsuzuki [142] proposed a new algorithm called “CoAnnealing”, whereby the concept of domination is mapped to classic “Energy Level” from traditional SA. CoAnnealing defined as an Energy Level of a point the largest domination (defined as MOSA’s domination) between the point and all points on the current Pareto front.

The Pareto front obtained through MOSA, CoAnnealing and the final solution from Single Objective Annealing is combined in Fig. 32. As observed, CoAnnealing front is broader than

MOSA, and completely dominates it. Also, while the single objective solution dominates some solutions from the MOSA Pareto front, it lies very close to the CoAnnealing Pareto Front.

The set of 20 images from CoAnnealing front is seen in Fig. 33. The measurement errors, insufficient information and modelling simplifications affect mostly the high frequencies components of the images. Thus a pure EIT reconstruction without any prior knowledge has noise in its high frequency components. Regularization dampens those coefficients. More regularized images have less noise, but some finer details of the image are lost. This approach allows for an expert to select the adequate amount of regularization *after* the reconstruction is done.

As for the execution time, CoAnnealing and MOSA have roughly the same performance (with an apparent small edge to CoAnnealing). The Energy Level proposed is expected to be used in the future with the *Partial Evaluation* technique proposed in [18] to reduce computational costs.

## 6. Clinical Applications of Time-Difference EIT

According to the current injection and reconstruction principles, EIT can be categorized to absolute EIT [14, 15] and difference EIT (including frequency-difference [3, 4] and time-difference EIT [5, 6]). Due to technical difficulties, only time-difference EIT is used in current commercial EIT devices and clinical applications [143]. The most commonly and well-developed thorax application is for patients in intensive care units (ICU) with ARDS [144]. Other clinical applications include patients with obstructive lung diseases [145] and perioperative patients [146].

### 6.1. Applications in ARDS Patients

The mortality rate of ARDS remains high, despite the recent improvements in disease management [147]. According to the therapeutic options in the Berlin definition of ARDS, PEEP should be applied to severe ARDS [148]. However, an appropriate “higher” PEEP is still uncertain [149, 150]. Individualized PEEP setting is considered useful in reducing lung damage caused by inappropriately high PEEP [151]. Recent clinical studies highlighted the potential use of EIT for ARDS in PEEP titration with or without recruitment maneuvers [152, 153, 154, 155, 156, 157, 158, 159, 160, 161, 162]. Lowhagen et al. [152] analyzed the changes of end-expiratory lung impedance (EELI) and intratidal ventilation distribution during PEEP changes. They found that these parameters could offer additional information to monitor recruitability and PEEP titration. The same group calibrated the impedance value to milliliter and calculated the potentially recruitable lung volume in each patient after the recruitment maneuver [153]. A considerable heterogeneity among the patients in lung recruitability was observed. The method is practical; however, the calibration of the impedance value must be conducted with caution, since the linearity between impedance and volume might not hold through out the vital capacity. Krueger-Ziolek et al. [163] found that during the vital capacity maneuver, the linearity between impedance and volume changed depending on the placement of electrode plane. The apparent non-linearity between impedance change and lung volume is most likely due to the lack of observability in the

Author Manuscript  
Author Manuscript  
Author Manuscript  
Author Manuscript  
Author Manuscript

craniocaudal direction caused by the electrode placement in a single plane. Karsten et al. [164] had similar findings in ICU patients. Spadaro et al. [160] evaluated poorly ventilated units of the dorsal lung region and found them correlated with lung recruitment measured by the pressure-volume curve. Long and his group explored the use of EIT identifying lung recruitability and optimal PEEP in combination with oxygenation [155, 156, 157]. They found that if oxygenation was not improved after the recruitment maneuver, it could be caused by lung tissue low recruitability or ventilation-perfusion mismatch. EIT may help to distinguish one cause from another to guide follow-up procedures [157]. Pulletz et al. [154] and Karagiannidis et al. [162] calculated the regional time constants, which may reflect the low respiratory system compliance and imply pronounced regional recruitment and derecruitment. Cinnella et al. [156] used EIT to prove that the application of the open lung approach in early mild ARDS would improve homogeneity in lung aeration. Recently in three independent prospective studies, EIT was used to select optimal PEEP at the bedside. In one study, PEEP was titrated with EELI level [159]. In two other studies, optimal PEEP was selected based on alveolar overdistension and alveolar collapse estimation derived from regional compliance [158, 161]. Even though the same measures were used in the latter studies, the selections of optimal PEEP were different. Franchineau et al. [158] studied severe ARDS patients with extracorporeal membrane oxygenation receiving very low tidal volume. Their optimal PEEP was defined as the lowest pressure able to limit EIT-assessed collapse to 15% with the least overdistension. The patient population in Heines et al. [161] study included mild, moderate and severe ARDS. Therefore, the criterion they used was to balance collapse and overdistension and selected the PEEP with the lowest sum of both. Many other EIT-based indices were developed and evaluated [146]. They may measure different aspects of ventilation distribution and the users have to choose the corresponding ones to serve their needs.

Other topics of EIT applications to ARDS include detection of pneumothorax [165], detection of patient-ventilator asynchrony [166] and lung perfusion [157]. Due to the time-difference nature in the commercial EIT devices, the detection of pneumothorax required a baseline to compare with. Therefore, EIT may be used to capture the appearance of pneumothorax or monitor its development, but not as a diagnosis tool [165]. Automatic detection of patient-ventilator asynchrony is a challenging task, since it is difficult to be revealed from pressure and flow curves. On the other hand, the asynchrony might be observed in the impedance curves of EIT measurements [166]. With the help of EIT, the attending physicians or respiratory therapists may focus on how to deal with the asynchrony, after identifying it [167]. Lung perfusion assessment by EIT in patients is usually performed with mathematical methods to separate cardiac related signals from ventilation signal. Although a more accurate technique would be using hypertonic saline as a contrast agent and analyzing the subsequent signal caused by the bolus injection [168, 169], to date, this technique is only applied to animals due to the high saline concentration.

## 6.2. Applications in Patients with Obstructive Lung Diseases

Patients with obstructive lung diseases often require routine pulmonary function tests (PFT) to monitor their disease progression. Traditional PFT provides only global information measured from the airway opening. Other techniques, such as multiple-breath washout

(MBW), require relative complex equipment and high cost. EIT offers a novel non-invasive way to assess regional lung function [170]. Zhao et al. [171] first applied EIT to measure regional lung function in cystic fibrosis (CF) patients. They validated in a small number of patients that EIT-derived measures are comparable to well-established CT-based scores [172]. Krueger-Ziolek et al. [173] explored the differences in regional lung function at different EIT electrode planes in CF and found that measurements at more cranial thorax planes may be more beneficial. The same group investigated whether normal tidal breathing could be used to substitute forced vital capacity maneuver in assessing lung function in CF [174]. They found that regional ventilation and cardiac-related pulsatile signals may help to identify breathing efforts and thus distinguish CF from healthy volunteers. These findings may also be applicable to patients with other obstructive lung diseases. Mueller et al. [108] used similar parameters to identify regions that are poorly ventilated but well perfused throughout the breathing and cardiac cycles. They compared these regions from two CF children to their chest CT and found that these regions were correlated to an air trapping area in CT images. The same group also used EIT to assess the response to intravenous antibiotic treatment for acute pulmonary exacerbations in CF [109]. Wettstein et al. [175] investigated the effect of breathing aids in CF patients and suggested that EIT might be used to individualize respiratory physiotherapy. As early as 1995, Eyübolu et al. [176] already used EIT to detect emphysema. Although at that time EIT technology was not well developed and the image quality was quite poor. Vogt et al. [145] evaluated spatial and temporal heterogeneity of ventilation in patients with chronic obstructive pulmonary disease (COPD) using EIT. The same group further tested regional lung response to bronchodilator reversibility in COPD [177] and asthma patients [178]. They also tested regional lung function in children before and after exercise challenge [179]. All these studies suggested that the EIT-derived regional lung parameters were stable and may be used to monitor the disease progression and treatments effects efficiently. However, reference values are still warranted to be established in order to make EIT a routine measurement in pulmonary function.

In the ICU, COPD patients with acute exacerbation (AECOPD) often require ventilator support. EIT provides quantitative assessment in regional lung ventilation guiding the ventilator settings. Frerichs et al. [180] evaluated the feasibility of applying high-frequency oscillatory ventilation (HFOV) to AECOPD. With help of EIT, they confirmed that ventilation was more homogeneously distributed during HFOV than during initial conventional mechanical ventilation. Sun et al. [181] examined the air distribution in AECOPD patients with neurally adjusted ventilatory assist (NAVA). They found that ventilation distribution in dependent regions increased significantly during NAVA as compared to pressure support ventilation (PSV). Besides, with EIT it is possible to assess the regional inspiration time [5] and expiratory time [162], as well as the regional distribution of air trapping to set external PEEP [182].

### 6.3. Applications in Perioperative Patients

Perioperative patients may have healthy lungs; however, guidelines for ventilation settings might not be well-established and might cause ventilator-induced lung injury [183]. It is feasible to use EIT to individualize tidal volume and PEEP before surgery [184, 185]. The influences of ventilation settings on patient outcomes were however not evaluated. During

capnoperitoneum in morbidly obese patients, EIT monitoring may guide the optimal PEEP adaptation [186]. Further, Nestler et al. [187] investigated the effect of recruitment and high PEEP on obese patients before and after surgery. They found that PEEP optimization helped to restore end-expiratory lung volume and to improve regional ventilation distribution. But the improvement did not persist after extubation. Therefore, they suggested that lung protection strategies should include the postoperative period. In another study with post-operative orthopedic patients, Radke et al. [188] examined the effect of trigger sensitivity on ventilation redistribution during PSV. Compared to spontaneous breathing, PSV induces a redistribution of ventilation towards the ventral region. The effect of trigger sensitivity could be revealed by EIT-based intratidal ventilation distribution. These findings coincided with those of the Taiwan group in studying prolonged mechanically ventilated (PMV) patients [189, 190]. In the study with 30 PMV patients, intratidal ventilation distribution was correlated to weaning outcome, which indicated that EIT has the potential to predict the weaning outcome and lower the extubation failure rate [190]. In twenty mechanically ventilated patients after elective cardiac surgery, Karsten et al. [191] found that the “best” PEEP value identified by individual maximum respiratory system compliance was lower than optimal PEEP levels determined by EIT. Since EIT provides regional information, the authors considered EIT to be a better option for PEEP titration. In a prospective study with children undergoing corrective open heart surgery, ventilation and cardiac-related impedance changes were measured with EIT before and after surgery [192]. EIT was able to measure the normalized ventilation to perfusion changes after the repair of a ventricular septum defect. In summary, EIT offers a new insight to provide guidance for perioperative ventilator settings.

## 7. Discussion and Future Works

A fair comparison among the proposed reconstruction methods presented here is difficult to be performed. The proposed methods have different maturity levels. By now, it is very difficult to assert which is the best reconstruction method. The anatomical atlas used in the G-N algorithm improved considerably the localization of organs on absolute images, as can be seen from Figs. 22 to 25. Improvement on the anatomical atlas is matter of investigation.

The SA-based and the UKF algorithms can be adapted to include the anatomical atlas as prior and some improvement is also expected. Bayesian filtering methods for EIT are heavily dependent on prior information due to the ill-posed nature of the problem. The construction of robust priors is key to success of these filters.

Evolution models of individuals in terms of impeditivity/conductivity distribution have strong potential. Kalman Filters require the estimation of the evolution model in a continuous manner. Another technological challenge comes from the fact that the FEM models of the thorax used in the inverse problem represent a truncated domain to minimize the computation time of the inverse problem. The boundary conditions of the truncation boundaries must be imposed consistently [20, 21]. Improvements on the boundary conditions on the truncation surfaces are investigation themes.

The main focus of the SA-based methods were the speedup, as it is the slower method among all. The incomplete evaluation of the objective function and massive parallelization acceleration are key features to make the SA-based methods clinically useful. However, the processing time is still long. The emergence of the outside-in property is an interesting behavior. The conductivities at the external layers can be computed first in a robust manner. This property can be useful if combined with other methods, including the D-Bar method. Such a combination is an investigation theme.

The MCMC reconstructions aims to obtain, more than a single image (e.g.: average or maximum *a posteriori* likelihood), the full probability distribution of the image. This is important as uncertainty information such as covariance are relevant for the interpretation of the image. Our approach to MCMC with partial objective function evaluation successfully obtains unbiased average images. Unfortunately, the covariance images may be biased by the incomplete evaluations, thus negating one of the important MCMC's advantages. An important future research topic is to estimate this bias and hopefully correct it, so that covariance data may be obtained even with incomplete objective function evaluations.

The D-bar method is the fastest among the presented methods. The D-bar method benefits from the prior information and possible usages of prior information with the D-bar method are investigation themes.

Multiobjective reconstruction of maximum *posterior* likelihood provide for, paradoxically, posterior selection of prior information weights, allowing experts to select the best values for their purposes. The CoAnnealing proposal allows the simultaneous optimization of *two* functions, leaving only one term for prior information. More sophisticated regularization techniques may add more terms with independent weights. For the use of such regularization, our CoAnnealing heuristics should be extended to more than two objective functions.

Due to the complexity and variability of biological systems, system identification methods should be employed to estimate evolution models in a continuous way [90, 89].

Measurement system uncertainty modeling is also of importance. In the clinic, correct electrode positioning and proper contact with the skin are challenging due to the patient's constant movement or manipulation. Methods to identify and compensate for faulty electrodes in real time and methods to mitigate electrode position errors have major impact. Biological tissue is known to be anisotropic [193] with capacitive properties [130], improve image quality.

Absolute images have more information than difference images, since the subtraction of two absolute images form one difference image conceptually. The clinical use of absolute images is potentially vast. Silent regions on difference images can be differentiated with absolute images. For instance, a silent pneumothorax is different from a silent atelectatic region in absolute image, or, a silent pleural effusion with cells is different from a silent pleural effusion with no cells. It will be possible to estimate silent gas volume, like FRC. It is likely that absolute images will be used routinely in medical environment and there already exists real time absolute images from Kalman Filters and D-Bar methods. Even non real time

methods for absolute images have their role in medical applications, some decisions can lag twenty or forty minutes.

The D-bar method has been used in some clinical studies. In [108], reconstructions by the D-bar method were used to compute ventilation-perfusion maps to identify regions of air trapping in two patients with cystic fibrosis, and the results were compared to computed tomography (CT) scans of the patients and to results from a healthy control. Global and regional EIT-derived spirometry measures were computed from D-bar reconstructions in [109] on 21 cystic fibrosis patients and 14 healthy controls, and the EIT measures demonstrated good correlation with spirometry and were able to distinguish between the cystic fibrosis patients and the healthy subjects. Since the D-bar method can provide real-time reconstructions, it is particularly suitable for bedside pulmonary imaging, where it remains to be clinically applied and tested. As with other methods, patient motion, uncertainty in electrode positioning, and poor electrode contact are detrimental to image quality. However, the study [128] demonstrates that absolute D-bar images can be surprisingly robust in the presence of errors in domain shape and electrode positioning. Efficient real-time methods of incorporating priors without biasing the images will have significant impact in the future.

The commercially available devices use time-difference technique to present the EIT images. This technique cannot reveal the actual volume in the regions of interest. When measurement conditions become different from the baseline, e.g. changes of skin condition, electrode position, thorax shape etc., baseline drift would be induced. Care should be taken when interpreting continuous long term EIT data, since some of the standard functional EITs would not be valid [5]. Although EIT has the potential to detect patient-ventilator asynchrony, diseases progression and to evaluate treatment efficiency, up to now there are no systematic studies exploring the feasibility and validity of long term EIT monitoring. Further investigations are necessary. Noted that measurement time longer than 24 hours on the same patient should be avoided due to potential risk of skin lesion. Another challenge for EIT clinical applications is that no well-documented guidelines are available in different scenarios instructing physicians and respiratory therapists how to use EIT. In order to establish guidelines, large randomized controlled trials should be conducted to prove the validity of the procedures, which are certainly one of the main directions of future work.

## 8. Conclusions

The control theory of linear time invariant systems can be invoked to optimize the hardware, electrode placement, current injection strategy and electric potential measurement strategy. A control theory-derived design criteria is to maximize the number of singular values of the transconductance matrix above the noise variance level.

The approximation error method minimizes the effects of using simplified or reduced models in the inversion problem. Careful modeling of the electrode is necessary and frequently the contact impedance must be estimated, electrode by electrode, simultaneously with the image estimation.

Even the most time consuming algorithms, SA-based algorithms, for absolute images should be further developed for two reasons, they are being speedup and the quality of the images should be addressed in a quantitative investigation. The hypothesis that methods that do not require the computation of gradients deliver higher quality images must be tested.

Physiological and anatomical priors, which appear naturally in a Bayesian framework for inverse problems, improve the localization of organs. An example of the development of an anatomical atlas for swines was described and the resulting images were presented. The composition of samples to form the anatomical atlas is object of research.

When the system is time varying, absolute images observability increases by the implementation of non-linear Kalman filters. The evolution model required by Kalman filters must be estimated at bedside and continuously. Most of the absolute image EIT algorithms are time-consuming, with the exception of D-Bar method and Kalman filters.

A review of medical applications of EIT revealed that three larger groups of applications standout: ARDS patients, perioperative patients and obstructive lung diseases.

## Acknowledgement

M. S. G. Tsuzuki, R. Gonzalez-Lima and T. C. Martins are partially supported by CNPq (respectively, Grants 305.959/2016–6, 306.415/2012–7 and 311.795/2016–1). A. K. Sato is supported by CAPES/PNPD. This project is supported by NIH (Grants 1R21EB009508-01A1 and 1R21EB02468301), CNPq (Grant 433.151/2018-8), FAPESP (Grants 2009/07173-2 and 2017/07799-5) and USP (NAP TIE-US). The protocol was approved by the Faculty of Medicine of the Universidade de São Paulo medical–ethics committee.

## Abbreviations

<b>AECOPD</b>	COPD Patient with Acute Exacerbation
<b>MOSA</b>	Algorithm Multi-Objective Simulated Annealing
<b>ARDS</b>	Acute Respiratory Distress Syndrome
<b>CEM</b>	Complete Electrode Model
<b>CF</b>	Cystic Fibrosis
<b>CG</b>	Conjugate Gradient
<b>CGO</b>	Complex Geometrical Optics
<b>COPD</b>	Chronic Obstructive Pulmonary Disease
<b>cpJDS</b>	Colored Padded Jagged Diagonal Storage
<b>CT</b>	Computerized Tomography
<b>cuBLAS</b>	Compute Unified Basic Linear Algebra Subprograms
<b>CUDA</b>	Compute Unified Device Architecture
<b>DN</b>	Dirichlet-to-Neumann

<b>EELI</b>	End-Expiratory Lung Impedance
<b>EIT</b>	Electrical Impedance Tomography
<b>FE</b>	Finite Element
<b>FEM</b>	Finite Element Methods
<b>G-N</b>	Gauss-Newton
<b>GM</b>	Gap Model
<b>GPGPU</b>	General Purpose Graphics Processing Unit
<b>GPU</b>	Graphics Processing Unit
<b>GQ</b>	Gaussian Quadrature
<b>HFOV</b>	High-Frequency Oscillatory Ventilation
<b>ICU</b>	Intensive Care Unit
<b>IEM</b>	Instrumental Electrode Model
<b>LA</b>	Lanczos Algorithm
<b>MAP</b>	Maximum a Posteriori
<b>MBW</b>	Multiple-Breath Washout
<b>MCMC</b>	Markov Chain Monte Carlo Method
<b>NAVA</b>	Neurally Adjusted Ventilatory Assist
<b>PDE</b>	Partial Differential Equation
<b>PDF</b>	Probability Density Function
<b>PEEP</b>	Positive End-Expiratory Pressure
<b>PEM</b>	Point Electrode Model
<b>PFT</b>	Pulmonary Function Tests
<b>pJDS</b>	Padded Jagged Diagonal Storage
<b>PMV</b>	Prolonged Mechanically Ventilated
<b>PSV</b>	Pressure Support Ventilation
<b>SA</b>	Simulated Annealing
<b>SA-CG</b>	SA-based method strongly based on the CG algorithm
<b>SA-CG-OIH</b>	SA-based method strongly based on the CG algorithm with outside-in heuristic

<b>SA-LB</b>	SA-based method strongly based on the LB algorithm
<b>SEM</b>	Shunt Electrode Model
<b>spMVM</b>	Sparse Vector-Matrix Multiplication
<b>UKF</b>	Unscented Kalman Filter

## References

- [1]. Carver B, Carver E, Medical imaging: techniques, reflection and evaluation, Elsevier, 2012.
- [2]. Bera TK, Nagaraju J, A multifrequency electrical impedance tomography (EIT) system for biomedical imaging, in: 2012 International Conference on Signal Processing and Communications (SPCOM), IEEE, 1–5, 2012.
- [3]. Santos SA, Czaplik M, Orschulik J, Hochhausen N, Leonhardt S, Lung pathologies analyzed with multi-frequency electrical impedance tomography: Pilot animal study, *Respiratory Physiology & Neurobiology* 254 (2018) 1–9. [PubMed: 29614341]
- [4]. Jang J, Seo JK, Detection of admittivity anomaly on high-contrast heterogeneous backgrounds using frequency difference EIT, *Physiological Measurement* 36 (6) (2015) 1179. [PubMed: 26008619]
- [5]. Zhao Z, Yun P-J, Kuo Y-L, Fu F, Dai M, Frerichs I, Miller K, Comparison of different functional EIT approaches to quantify tidal ventilation distribution, *Physiological Measurement* 39 (1) (2018) 01NT01.
- [6]. Gong B, Krueger-Ziolek S, Moeller K, Schullcke B, Zhao Z, Electrical impedance tomography: functional lung imaging on its way to clinical practice?, *Expert Review of Respiratory Medicine* 9 (6) (2015) 721–737. [PubMed: 26488464]
- [7]. Brown BH, Electrical impedance tomography (EIT): a review, *Journal of Medical Engineering & Technology* 27 (3) (2003) 97–108. [PubMed: 12775455]
- [8]. Grychtol B, Elke G, Meybohm P, Weiler N, Frerichs I, Adler A, Functional validation and comparison framework for EIT lung imaging, *PLoS One* 9 (8) (2014) e103045. [PubMed: 25110887]
- [9]. Kao TJ, Isaacson D, Newell JC, Saulnier GJ, A 3D reconstruction algorithm for EIT using a handheld probe for breast cancer detection, *Physiological Measurements* 27 (2006) S1–S11.
- [10]. Clay MT, Frree TC, Weighted regularization in electrical impedance tomography with applications to acute cerebral stroke, *IEEE Transactions on Medical Imaging* 21 (2002) 629–637. [PubMed: 12166859]
- [11]. Eyübüglü BM, Brown BH, Barber DC, In vivo imaging of cardiac related impedance changes, *IEEE Engineering in Medicine and Biology Magazine* 8 (1989) 39–45. [PubMed: 18238304]
- [12]. Trigo FC, Lima RG, Amato MBP, Electrical impedance tomography using the extended Kalman filter, *IEEE Transactions on Biomedical Engineering* 51 (2004) 72–81. [PubMed: 14723496]
- [13]. Hua P, Woo E, Webster JG, Tompkins WJ, Finite element modeling of electrode-skin contact impedance in electrical impedance tomography, *IEEE Transactions on Biomedical Engineering* 40 (4) (1993) 335–343. [PubMed: 8375870]
- [14]. Denai MA, Mahfouf M, Mohamad-Samuri S, Panoutsos G, Brown BH, Mills GH, Absolute electrical impedance tomography (aEIT) guided ventilation therapy in critical care patients: simulations and future trends, *IEEE Transactions on Information Technology in Biomedicine* 14 (3) (2010) 641–649. [PubMed: 19906599]
- [15]. Zhang J, Patterson R, Non-invasive determination of absolute lung resistivity in adults using electrical impedance tomography, *Physiological Measurement* 31 (8) (2010) S45. [PubMed: 20647615]
- [16]. Holder D, Institute of Physics (Great Britain), Electrical impedance tomography: methods, history, and applications, Institute of Physics Pub, 2005.

- [17]. Tavares RS, Sato AK, Martins TC, Lima RG, Tsuzuki MSG, GPU acceleration of absolute EIT image reconstruction using simulated annealing, *Biomedical Signal Processing and Control* (2017) 10.1016/j.bspc.2017.02.007.
- [18]. Martins TC, Camargo EDLB, Lima RG, Amato MBP, Tsuzuki MSG, Image reconstruction using interval simulated annealing in electrical impedance tomography, *IEEE Transactions on Biomedical Engineering* 59 (7) (2012) 1861–1870. [PubMed: 22361655]
- [19]. Martins TC, Tsuzuki MSG, de Camargo EDLB, Lima RG, de Moura FS, Amato MBP, Interval Simulated Annealing applied to Electrical Impedance Tomography image reconstruction with fast objective function evaluation, *Computers & Mathematics with Applications* 72 (5) (2016) 1230–1243.
- [20]. Calvetti D, Hadwin PJ, Huttunen JMJ, Isaacson D, Kaipio JP, McGivney D, Somersalo E, Volzer J, Artificial boundary conditions and domain truncation in electrical impedance tomography. Part I: Theory and preliminary results, *Inverse Problems and Imaging* 9 (3) (2015) 749–766.
- [21]. Calvetti D, Hadwin PJ, Huttunen JMJ, Kaipio JP, Somersalo E, Artificial boundary conditions and domain truncation in electrical impedance tomography. Part II: Stochastic extension of the boundary map, *Inverse Problems and Imaging* 9 (3) (2015) 767–789, ISSN 1930–8337.
- [22]. Kaipio JP, Somersalo E, Statistical inverse problems: Discretization, model reduction and inverse crimes, *Journal of Computational and Applied Mathematics* 198 (2) (2007) 493–504, special Issue: Applied Computational Inverse Problems.
- [23]. Kaipio JP, Somersalo E, Statistical and computational inverse problems, vol. 160, Springer, 2004.
- [24]. Dodd M, Mueller JL, A real-time D-bar algorithm for 2-D electrical impedance tomography data, *Inverse Probl. Imag* 8 (4) (2014) 1013–1031.
- [25]. Hamilton SJ, Mueller JL, Alsaker M, Incorporating a Spatial Prior into Nonlinear D-Bar EIT Imaging for Complex Admittivities, *IEEE T. Med. Imaging* 36 (2) (2017) 457–466.
- [26]. Silva OL, Lima RG, Martins TC, Moura FS, Tavares RS, Tsuzuki MSG, Influence of current injection pattern and electric potential measurement strategies in electrical impedance tomography, *Control Engineering Practice* 58 (2017) 276–286.
- [27]. Adler A, Amato MBP, Arnold JH, Bayford R, Bodenstein M, Böhm SH, Brown BH, Frerichs I, Stenqvist O, Weiler N, Wolf GK, Whither lung EIT: Where are we, where do we want to go and what do we need to get there?, *Physiological Measurement* 33 (5) (2012) 679–694, ISSN 0967–3334. [PubMed: 22532268]
- [28]. Camargo EDLB, Desenvolvimento de algoritmo de imagens absolutas de Tomografia por Impedância Elétrica para uso clínico, Phd thesis, Escola Politécnica da Universidade de São Paulo, São Paulo, 2013.
- [29]. Brown BH, Seagar A, The Sheffield data collection system, *Clinical Physics and Physiological Measurements* 8 (1987) A91–A97.
- [30]. Hua P, Webster JG, Tompkins WJ, A regularised electrical impedance tomography reconstruction algorithm, *Clinical Physics and Physiological Measurements* 9 (1988) 137–141.
- [31]. Cheney M, Isaacson D, Newell JC, Electrical Impedance Tomography, *SIAM Review* 41 (1) (1999) 85–101.
- [32]. Demidenko E, Hartov A, Soni N, Paulsen KD, On optimal current patterns for electrical impedance tomography, *IEEE Transactions on Biomedical Engineering* 52 (2) (2005) 238–248. [PubMed: 15709661]
- [33]. Lionheart WRB, Kaipio JP, McLeod CN, Generalized optimal current patterns and electrical safety in EIT, *Physiological Measurement* 22 (1) (2001) 85–90. [PubMed: 11236893]
- [34]. Geddes LA, Costa CP, Wise G, The impedance of stainless-steel electrodes, *Medical and biological engineering* 9 (5) (1971) 511–521. [PubMed: 5159049]
- [35]. Pollak V, Computation of the impedance characteristic of metal electrodes for biological investigations, *Medical and biological engineering* 12 (4) (1974) 460–464. [PubMed: 4465562]
- [36]. Bockris JOM, Reddy AKN, Gamboa-Aldeco M, *Modern Electrochemistry: Fundamentals of Electrodics*. V. 2a, Plenum Press, 1998.
- [37]. Lionheart W, Polydorides N, Borsic A, The reconstruction problem, in: Holder D (Ed.), *Electrical Impedance Tomography: Methods, History and Applications*, Institute of Physics Publishing, Bristol and Philadelphia, 1st edn., ISBN 0–7503–0952–0, 3,64, 2005.

- [38]. Cheng K-S, Isaacson D, Newell JC, Gisser DG, Electrode models for electric current computed tomography, *IEEE Transactions on Biomedical Engineering* 36 (9) (1989) 918–924. [PubMed: 2777280]
- [39]. Hanke M, Harrach B, Hyvönen N, Justification of point electrode models in electrical impedance tomography, *Mathematical Models and Methods in Applied Sciences* 21 (06) (2011) 1395–1413.
- [40]. Hanke M, Brühl M, Recent progress in electrical impedance tomography, *Inverse Problems* 19 (6) (2003) S65.
- [41]. Somersalo E, Cheney M, Isaacson D, Existence and uniqueness for electrode models for electric current computed tomography, *SIAM Journal on Applied Mathematics* 52 (4) (1992) 1023–1040.
- [42]. Paulson K, Breckon W, Pidcock M, Electrode modelling in electrical impedance tomography, *SIAM Journal on Applied Mathematics* 52 (4) (1992) 1012–1022.
- [43]. Vauhkonen PJ, Vauhkonen M, Savolainen T, Kaipio JP, Three-dimensional electrical impedance tomography based on the complete electrode model, *IEEE Transactions on Biomedical Engineering* 46 (9) (1999) 1150–1160. [PubMed: 10493078]
- [44]. Vilhunen T, Kaipio JP, Vauhkonen PJ, Savolainen T, Vauhkonen M, Simultaneous reconstruction of electrode contact impedances and internal electrical properties: I. Theory, *Measurement Science and Technology* 13 (12) (2002) 1848.
- [45]. Dardé J, Hyvönen N, Seppänen A, Staboulis S, Simultaneous recovery of admittivity and body shape in electrical impedance tomography: An experimental evaluation, *Inverse Problems* 29 (8) (2013) 085004.
- [46]. Dardé J, Staboulis S, Electrode modelling: The effect of contact impedance, *ESAIM: Mathematical Modelling and Numerical Analysis* 50 (2) (2016) 415–431.
- [47]. Hyvonen N, Mustonen L, Smoothed complete electrode model, *SIAM Journal on Applied Mathematics* 77 (6) (2017) 2250–2271.
- [48]. Zhang W, Li D, An instrumental electrode model for solving EIT forward problems, *Physiological Measurement* 35 (10) (2014) 2001–2026. [PubMed: 25238259]
- [49]. Silva OL, Muscle contraction detection using electrical impedance tomography, Phd thesis, Escola Politécnica da Universidade de São Paulo, São Paulo, 2012.
- [50]. Silva OL, Lima RG, Numerical Convergence of 3D Electrode Models used in Electrical Impedance Tomography, *IFAC-PapersOnLine* 51 (27) (2018) 30–35.
- [51]. Sato AK, Bianchessi A, Martins TC, Lima RG, Tsuzuki MSG, A new 2D dual layered electrode model for the electrical impedance tomography, *IFAC-PapersOnLine* 51 (2018) 41–46.
- [52]. Tavares RS, Nakadaira-Filho FA, Tsuzuki MSG, Martins TC, Lima RG, Discretization error and the EIT forward problem, *IFAC-PapersOnLine* 47 (3) (2014) 7535–7540, ISSN 1474–6670, 19th IFAC WC.
- [53]. Kreutzer M, Hager G, Wellein G, Fehske H, Basermann A, Bishop AR, Sparse matrix-vector multiplication on GPGPU clusters: a new storage format and a scalable implementation, in: 2012 IEEE 26th International Parallel and Distributed Processing Symposium Workshops & PhD Forum, 1696–1702, 2012.
- [54]. Vázquez F, Fernández JJ, Garzón EM, A new approach for sparse matrix vector product on NVIDIA GPUs, *Concurrency and computation: practice and experience* 23 (8) (2011) 815–826.
- [55]. Ogata K, *Discrete-time Control Systems*, Prentice-Hall, Inc., Upper Saddle River, NJ, USA, 1987.
- [56]. Yang C-D, Yeh F-B, Identification, reduction, and refinement of model parameters by the eigensystem realization algorithm, *Journal of Guidance Control and Dynamics - J GUID CONTROL DYNAM* 13 (1990) 1051–1059.
- [57]. Nissinen A, Kolehmainen V, Kaipio JP, Reconstruction of domain boundary and conductivity in electrical impedance tomography using the approximation error approach, *International Journal for Uncertainty Quantification* 1 (3) (2011) 203–222.
- [58]. Lipponen A, Seppänen A, Kaipio JP, Nonstationary approximation error approach to imaging of three-dimensional pipe flow: experimental evaluation, *Measurement Science and Technology* 22 (10) (2011) 104013.
- [59]. Siltanen S, Mueller J, Isaacson D, An implementation of the reconstruction algorithm of A. Nachman for the 2-D inverse conductivity problem, *Inverse Problems* 16 (2000) 681–699.

- [60]. Nachman AI, Global uniqueness for a two-dimensional inverse boundary value problem, *Annals of Mathematics* 143 (1996) 71–96.
- [61]. Martins TC, Camargo EDLB, Lima RG, Amato MBP, Tsuzuki MSG, Electrical impedance tomography reconstruction through simulated annealing with incomplete evaluation of the objective function., in: Proceedings of the 33th IEEE Annual International Engineering in Medicine and Biology Conference, Boston, USA, 7033–7036, 2011.
- [62]. Martins TC, Tsuzuki MSG, Simulated annealing with partial evaluation of objective function applied to electrical impedance tomography, in: Proceedings of the 18th IFAC World Congress, Milano, Italy, 4989–4994, 2011.
- [63]. Meurant G, Estimates of the l2 norm of the error in the conjugate gradient algorithm, *Numerical Algorithms* 40 (2005) 157–169.
- [64]. Somersalo E, Cheney M, Isaacson D, Isaacson E, Layer stripping: a direct numerical method for impedance imaging, *Inverse Problems* 7 (6) (1991) 899–926.
- [65]. Tavares RS, Martins TC, Tsuzuki MSG, Electrical Impedance Tomography Reconstruction Through Simulated Annealing using a New Outside-in Heuristic and GPU Parallelization, *Journal of Physics: Conference Series* 407 (1) (2012) 012015.
- [66]. Meurant G, The Lanczos and conjugate gradient algorithms: from theory to finite precision computations, SIAM, 2006.
- [67]. Martins TC, Tsuzuki MSG, Electrical Impedance Tomography Reconstruction Through Simulated Annealing with Total Least Square Error as Objective Function, in: Proceedings of the 34th IEEE Annual International Engineering in Medicine and Biology Conference, San Diego, USA, 1518–1521, 2012.
- [68]. Vauhkonen PJ, Vauhkonen M, Kaipio JP, Errors due to the truncation of the computational domain in static three-dimensional electrical impedance tomography, *Physiol Meas* 21 (1) (2000) 125–135. [PubMed: 10720008]
- [69]. Golub GH, Meurant G, Matrices, Moments and quadrature with applications, Princeton University Press, 2010.
- [70]. Martins TC, Tsuzuki MSG, Electrical Impedance Tomography Reconstruction Through Simulated Annealing with Multi-Stage Partially Evaluated Objective Functions., in: Proceedings of the 35th IEEE Annual International Engineering in Medicine and Biology Conference, Osaka, Japan, 6425–6428, 2013.
- [71]. Metropolis N, Rosenbluth AW, Rosenbluth MN, Teller AH, Teller E, Equation of state calculations by fast computing machines, *Journal of Chemical Physics* 21 (1953) 1087–1092.
- [72]. Alquier P, Friel N, Everitt R, Boland A, Noisy Monte Carlo: Convergence of Markov Chains with Approximate Transition Kernels, *Statistics and Computing* 26 (1–2) (2016) 29–47.
- [73]. Martins TC, Tsuzuki MSG, Markov Chain Monte Carlo electrical impedance tomography reconstruction through intervalar evaluation, *IFAC-PapersOnLine* 51 (27) (2018) 47–51.
- [74]. Björck A, Numerical methods for least squares problems, Society for Industrial and Applied Mathematics, 1996.
- [75]. Vauhkonen PJ, Image reconstruction in three-dimensional electrical impedance tomography, Phd thesis, University of Kuopio, 2004.
- [76]. de Lima CR, Mello LAM, Lima RG, Silva ECN, Electrical impedance tomography through constrained sequential linear programming: a topology optimization approach, *Measurement Science and Technology* 18 (2007) 2847–2858.
- [77]. Adler A, Guardo R, Electrical impedance tomography: regularized imaging and contrast detection, *IEEE Transactions on Medical Imaging* 15 (2) (1996) 170–179. [PubMed: 18215899]
- [78]. Borsic A, Graham BM, Adler A, Lionheart WRB, In vivo impedance imaging with total variation regularization, *IEEE Transactions on Medical Imaging* 29 (1) (2010) 44–54. [PubMed: 20051330]
- [79]. Kaipio JP, Kolehmainen V, Vauhkonen M, Somersalo E, Construction of anatomy-based priors with anisotropic characteristics with application to electrical impedance tomography, in: Proceedings of the 20th Annual International Conference of the IEEE Engineering in Medicine and Biology Society, vol. 20, IEEE, Hong Kong, China, 1032–1035, 1998.

- [80]. Gabriel S, Lau RW, Gabriel C, The dielectric properties of biological tissues: II. Measurements in the frequency range 10 Hz to 20 GHz, *Physics In Medicine And Biology* 41 (1996) 2251–2269. [PubMed: 8938025]
- [81]. Sousa T, Moura I, Hoffmann F aS nd, Camargo EDLB, Lima RG, Martins A, Fantoni D, Biasi C, In vivo admittivity measurements for regularizations in electrical impedance tomography, in: Proceedings of COBEM 2011, 21st International Congress of Mechanical Engineering, 24–28, 2011.
- [82]. Vauhkonen M, Karjalainen PA, Kaipio JP, A Kalman Filter Aproach to Track Fast Impedance Changes in Electrical Impedance Tomography, *IEEE Transactions on Biomedical Engineering* 45 (4) (1998) 486–493. [PubMed: 9556965]
- [83]. Kim KY, Kim BS, Kim MC, Lee YJ, Vauhkonen M, Image Reconstruction in Time-varying Electrical Impedance Tomography Based on The Extended Kalman Filter, *Measurement Science and Technology* 12 (8) (2001) 1032–1039.
- [84]. Kim KY, Kang SI, Kim MC, Kim S, Lee YJ, Vauhkonen M, Dynamic Image Reconstruction in Electrical Impedance Tomography With Known Internal Structure, *IEEE Transactions on Magnetics* 38 (2) (2002) 1301–1304.
- [85]. Kim BS, Kim MC, Kim S, Kim KY, Nonstationary electrical impedance tomography with the interacting multiple model scheme, *Measurement Science and Technology* 15 (10) (2004) 2113–2123.
- [86]. Kolehmainen V, Voutilainen A, Kaipio JP, Estimation of non-stationary region boundaries in EIT-state estimation approach, *Inverse Problems* 17 (6) (2001) 1937–1956.
- [87]. Kaipio JP, Karjalainen PA, Somersalo E, State Estimation in Time-Varying Electrical Impedance Tomography, *Annals of the New York Academy Of Sciences* 873 (1999) 430–439.
- [88]. Trigo FC, Estimação não linear de parâmetros através dos filtros de Kalman na tomografia por impedância elétrica, Ph.D. thesis, Escola Politécnica da Universidade de São Paulo, São Paulo, 2005.
- [89]. Moura FS, Aya JCC, Fleury AT, Amato MBP, Lima RG, Dynamic Imaging in Electrical Impedance Tomography of the Human Chest With Online Transition Matrix Identification, *IEEE Transactions on Biomedical Engineering* 57 (2) (2010) 422–431. [PubMed: 19789101]
- [90]. Moura FS, Estimação não linear de estado através do Unscented Kalman Filter na tomografia por impedância elétrica, Phd thesis, Escola Politécnica da Universidade de São Paulo, São Paulo, 2013.
- [91]. Nelson L, Stear E, The simultaneous on-line estimation of parameters and states in linear systems, *IEEE Transactions on Automatic Control* 21 (1) (1976) 94–98.
- [92]. Venegas JG, Harris RS, Simon BA, A comprehensive equation for the pulmonary pressure-volume curve, *Journal of Applied Physiology* 84 (1) (1998) 389–395. [PubMed: 9451661]
- [93]. Bates JHT, Lung Mechanics: An Inverse Modeling Approach, Cambridge University Press, 1 edn., 2009.
- [94]. Liu CH, Nirajan SC, J. C. J. W., San KY, Zwischenberger JB, Bidani A, Airway mechanics, gas exchange, and blood flow in a nonlinear model of the normal human lung, *Journal of Applied Physiology* 84 (4) (1998) 1447–1469. [PubMed: 9516216]
- [95]. Bates JHT, Irvin CG, Time dependence of recruitment and derecruitment in the lung: a theoretical model, *Journal of Applied Physiology* 93 (2) (2002) 705–713. [PubMed: 12133882]
- [96]. Kaminsky DA, Irvin CG, Lundblad L, Moriya HT, Lang S, Allen J, Viola T, Lynn M, Bates JHT, Oscillation mechanics of the human lung periphery in asthma, *Journal of Applied Physiology* 97 (2004) 1849–1858. [PubMed: 15220299]
- [97]. Allen GB, Pavone LA, DiRocco JD, Bates JHT, Nieman GF, Pulmonary impedance and alveolar instability during injurious ventilation in rats, *Journal of Applied Physiology* 99 (2) (2005) 723–730. [PubMed: 15831795]
- [98]. Nopp P, Harris ND, Zhao TX, Brown BH, Model for the dielectric properties of human lung tissue against frequency and air content, *Medical and Biological Engineering and Computing* 35 (6) (1997) 695–702. [PubMed: 9538548]

- [99]. Li C, Xu C, Gui C, Fox MD, Level Set Evolution Without Reinitialization: A New Variational Formulation, in: Proceedings of the 2005 IEEE Computer Society Conference on Computer Vision and Pattern Recognition, vol. 1, 430–436, 2005.
- [100]. Calderón AP, On an inverse boundary value problem, in: Seminar on Numerical Analysis and its Applications to Continuum Physics (Rio de Janeiro, 1980), Soc. Brasil. Mat., Rio de Janeiro, 65–73, 1980.
- [101]. Mueller JL, Siltanen S, Linear and Nonlinear Inverse Problems with Practical Applications, SIAM, 2012.
- [102]. Novikov RG, A multidimensional inverse spectral problem for the equation  $-\psi''(v(x))\psi = 0$ , Functional Analysis and Its Applications 22 (4) (1988) 263–272.
- [103]. Nachman AI, Reconstructions from boundary measurements, Annals of Mathematics 128 (1988) 531–576.
- [104]. Isaacson D, Mueller JL, Newell JC, Siltanen S, Reconstructions of chest phantoms by the D-bar method for electrical impedance tomography, IEEE T. Med. Imaging 23 (7) (2004) 821–828.
- [105]. Isaacson D, Mueller JL, Newell JC, Siltanen S, Imaging cardiac activity by the D-bar method for electrical impedance tomography, Physiol. Meas 27 (5) (2006) S43–S50. [PubMed: 16636419]
- [106]. Knudsen K, Lassas M, Mueller JL, Siltanen S, Regularized D-bar method for the inverse conductivity problem, Inverse Problems and Imaging 3 (4) (2009) 599–624.
- [107]. Murphy EK, Mueller JL, Effect of domain-shape modeling and measurement errors on the 2-D D-bar method for electrical impedance tomography, IEEE Transactions on Medical Imaging 28 (10) (2009) 1576–1584. [PubMed: 19447702]
- [108]. Mueller JL, Muller P, Mellenthin M, Murthy R, Capps M, Alsaker M, Deterding R, Sagel SD, Deboer E, Estimating regions of air trapping from electrical impedance tomography data, Physiological Measurement 39 (5) (2018) 05NT01.
- [109]. Muller PA, Mueller JL, Mellenthin M, Murthy R, Capps M, Wagner BD, Alsaker M, Deterding R, Sagel SD, Hoppe J, Evaluation of surrogate measures of pulmonary function derived from electrical impedance tomography data in children with cystic fibrosis, Physiological Measurement 39 (4) (2018) 045008. [PubMed: 29565263]
- [110]. Cornean H, Knudsen K, Siltanen S, Towards a  $d$ -bar reconstruction method for three-dimensional EIT, Journal of Inverse and Ill-Posed Problems 14 (2) (2006) 111–134, ISSN 0928–0219.
- [111]. Bikowski J, Knudsen K, Mueller JL, Direct numerical reconstruction of conductivities in three dimensions using scattering transforms, Inverse Problems 27.
- [112]. Delbary F, H. P. C., Knudsen K, A direct numerical reconstruction algorithm for the 3D Calderón problem, in: Journal of Physics: Conference Series, vol. 290, IOP Publishing, 0120003, 2011.
- [113]. Knudsen K, Mueller JL, The Born approximation and Calderón’s method for reconstructions of conductivities in 3-D, Discrete and Continuous Dynamical Systems (2011) 884–893.
- [114]. Delbary F, Hansen PC, Knudsen K, Electrical impedance tomography: 3D reconstructions using scattering transforms, Applicable Analysis 0 (0) (0) 1–19.
- [115]. Delbary F, Knudsen K, Full numerical implementation of the scattering transform algorithm for the 3D Calderón problem, Inverse Problems and Imaging.
- [116]. Adams RA, Sobolev Spaces, Academic Press, 1975.
- [117]. Faddeev LD, Increasing Solutions of the Schroedinger Equation, Sov. Phys. Dokl 10 (1966) 1033–1035.
- [118]. Siltanen S, Electrical impedance tomography and Faddeev Green’s functions, Annales Academiae Scientiarum Fennicae Mathematica Dissertationes 121 (121) (1999) 56, ISSN 1239–6303, dissertation, Helsinki University of Technology, Espoo, 1999.
- [119]. Muller PA, Numerical Methods for Electrical Impedance Tomography, Ph.D. thesis, Rensselaer Polytechnic Institute, Troy, NY, 2014.
- [120]. Mueller JL, Siltanen S, Direct reconstructions of conductivities from boundary measurements, SIAM Journal on Scientific Computing 24 (4) (2003) 1232–1266.

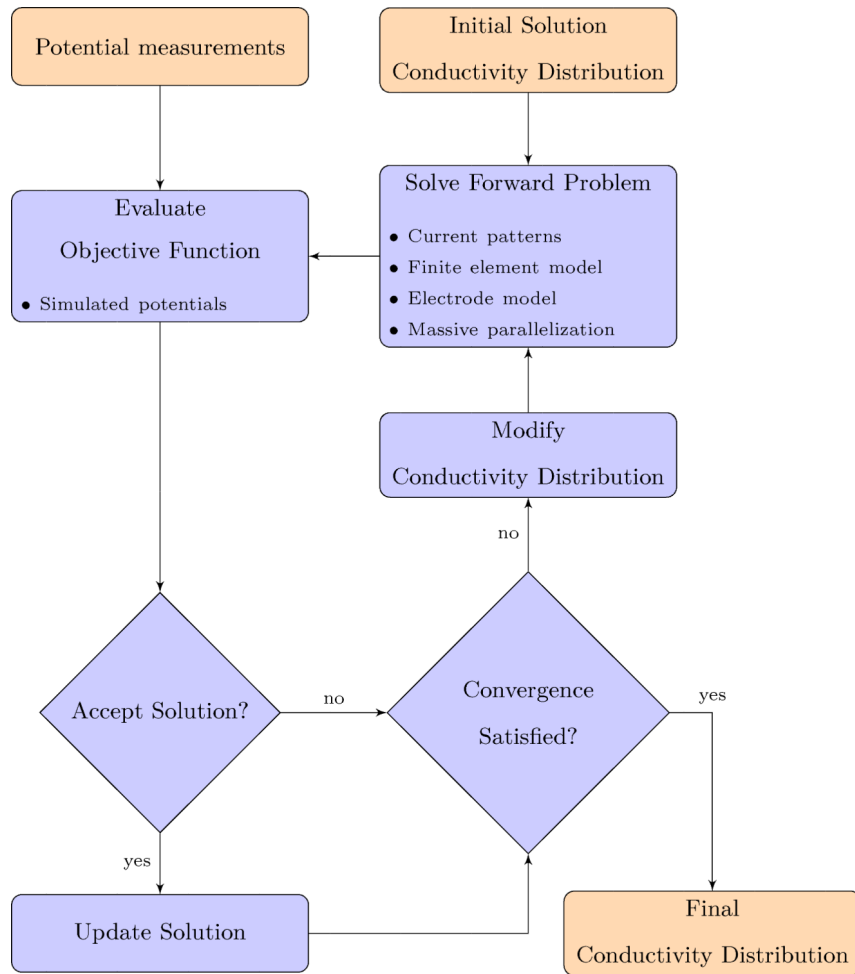
- [121]. DeAngelo M, Mueller JL, 2D D-bar reconstructions of human chest and tank data using an improved approximation to the scattering transform, *Phys. Meas.* 31 (2) (2010) 221–232.
- [122]. Mellenthin MM, Mueller JL, de Camargo EDLB, de Moura FS, Santos TBR, Lima RG, Hamilton SJ, Muller PA, Alsaker M, The ACE1 Electrical Impedance Tomography System for Thoracic Imaging, *IEEE Transactions on Instrumentation and Measurement*.
- [123]. Hamilton SJ, Herrera CNL, Mueller JL, VonHerrmann A, A Direct D-bar Reconstruction Algorithm for Recovering a Complex Conductivity in 2-D, *Inverse Problems* 28:(095005).
- [124]. Alsaker M, Mueller JL, A D-Bar algorithm with A priori information for 2-dimensional electrical impedance tomography, *SIAM J. Imaging Sci* 9 (4) (2016) 1619–1654.
- [125]. Alsaker M, Mueller JL, Use of an optimized spatial prior in D-bar reconstructions of EIT tank data, *Inverse Problems and Imaging* 12 (4) (2018) 883–901.
- [126]. Alsaker M, Hamilton SJ, Hauptmann A, A Direct D-bar method for partial boundary data electrical impedance tomography with A priori information, *Inverse Problems and Imaging* (accepted).
- [127]. Alsaker M, Mueller JL, Murthy R, Dynamic optimized priors for D-bar reconstructions of human ventilation using electrical impedance tomography, *Journal of Computational and Applied Mathematics* (2018) to appear.
- [128]. Hamilton SJ, Mueller JL, Santos T, Robust computation of 2D EIT absolute images with D-bar methods, *Physiological Measurement* 39 (2018) 064005. [PubMed: 29846182]
- [129]. Herrera CNL, Um metodo D-bar para estimar admitividade em 2-D atraves de tomografia por impedancia electrica, Ph.D. Thesis, University of São Paulo, São Paulo, Brazil, 2012.
- [130]. Herrera CNL, Vallejo MFM, Mueller JL, Lima RG, Direct 2-D Reconstructions of Conductivity and Permittivity From EIT Data on a Human Chest, *IEEE T. Med. Imaging* 34 (1) (2015) 267–274.
- [131]. Francini E, Recovering a complex coefficient in a planar domain from the Dirichlet-to-Neumann map, *Inverse Problems* 16 (2000) 107–119.
- [132]. Brown RM, Uhlmann G, Uniqueness in the inverse conductivity problem for nonsmooth conductivities in two dimensions, *Communications in Partial Differential Equations* 22 (5) (1997) 1009–1027.
- [133]. Hamilton SJ, EIT Imaging of admittivities with a D-bar method and spatial prior: experimental results for absolute and difference imaging, *Physiological Measurement* 38 (6) (2017) 1176–1192. [PubMed: 28530208]
- [134]. Knudsen K, Lassas M, Mueller JL, Siltanen S, D-bar method for electrical impedance tomography with discontinuous conductivities, *SIAM Journal on Applied Mathematics* 67 (3) (2007) 893.
- [135]. Bikowski J, Mueller J, 2D EIT reconstructions using Calderón’s method, *Inverse Problems and Imaging* 2 (1) (2008) 43–61.
- [136]. Muller PA, Mueller JL, Mellenthin M, Real-time implementation of Calderón’s method on subject-specific domains, *IEEE Transactions on Medical Imaging* 36 (9) (2017) 1868–1875. [PubMed: 28436855]
- [137]. Jones DF, Mirrazavi SK, Tamiz M, Multi-objective meta-heuristics: An overview of the current state-of-the-art, *European Journal of Operational Research* 137 (2002) 1–9.
- [138]. Suppapitnarm A, Seffen KA, Parks GT, Clarkson PJ, A Simulated Annealing Algorithm for Multiobjective Optimization, *Engineering Optimization* 33 (2000) 59–85.
- [139]. Ngatchou P, Zarei A, El-Sharkawi A, Pareto Multi Objective Optimization, in: Proceedings of the 13th International Conference on Intelligent Systems Application to Power Systems, 84–91, 2005.
- [140]. Martins TC, Fernandes AV, Tsuzuki MSG, Image reconstruction by electrical impedance tomography using multi-objective simulated annealing, in: IEEE 11th International Symposium on Biomedical Imaging, Beijing, China, 185–188, 2014.
- [141]. Engrand P, A multi-objective approach based on simulated annealing and its application to nuclear fuel management, in: 5th International Conference on Nuclear Engineering, Nice, France, 1–8, 1997.

- [142]. Martins TC, Tsuzuki MSG, EIT image regularization by a new Multi-Objective Simulated Annealing algorithm, in: Proceedings of the 37th IEEE Annual International Engineering in Medicine and Biology Conference, Milan, Italy, 4069–4072, 2015.
- [143]. Frerichs I, Amato MBP, van Kaam AH, Tingay DG, Zhao Z, Grychtol B, Bodenstein M, Gagnon H, Böhm SH, Teschner E, Stenqvist O, Mauri T, Torsani V, Camporota L, Schibler A, Wolf GK, Gommers D, Leonhardt S, Adler A, Chest electrical impedance tomography examination, data analysis, terminology, clinical use and recommendations: consensus statement of the TRanslational EIT developmeNt stuDy group, *Thorax* 72 (1) (2017) 83–93. [PubMed: 27596161]
- [144]. Bachmann MC, Morais C, Buggedo G, Bruhn A, Morales A, Borges JB, Costa E, Retamal J, Electrical impedance tomography in acute respiratory distress syndrome, *Critical Care* 22 (1) (2018) 263. [PubMed: 30360753]
- [145]. Vogt B, Pulletz S, Elke G, Zhao Z, Zabel P, Weiler N, Frerichs I, Spatial and temporal heterogeneity of regional lung ventilation determined by electrical impedance tomography during pulmonary function testing, *Journal of Applied Physiology* 113 (7) (2012) 1154–1161. [PubMed: 22898553]
- [146]. Frerichs I, Hahn G, Golisch W, Kurpitz M, Burchardi H, Hellige G, Monitoring perioperative changes in distribution of pulmonary ventilation by functional electrical impedance tomography, *Acta Anaesthesiologica Scandinavica* 42 (6) (1998) 721–726. [PubMed: 9689281]
- [147]. Pham T, Rubenfeld GD, Fifty Years of Research in ARDS. The Epidemiology of Acute Respiratory Distress Syndrome. A 50th Birthday Review, *American Journal of Respiratory and Critical Care Medicine* 195 (7) (2017) 860–870. [PubMed: 28157386]
- [148]. Ferguson ND, Fan E, Camporota L, Antonelli M, Anzueto A, Beale R, Brochard L, Brower R, Esteban A, Gattinoni L, Rhodes A, Slutsky AS, Vincent J-L, Rubenfeld GD, Thompson BT, Ranieri VM, The Berlin definition of ARDS: an expanded rationale, justification, and supplementary material, *Intensive Care Medicine* 38 (10) (2012) 1573–1582. [PubMed: 22926653]
- [149]. Brower RG, Lanken PN, MacIntyre N, Matthay MA, Morris A, Ancukiewicz M, Schoenfeld D, Thompson BT, Higher versus Lower Positive End-Expiratory Pressures in Patients with the Acute Respiratory Distress Syndrome, *New England Journal of Medicine* 351 (4) (2004) 327–336. [PubMed: 15269312]
- [150]. Meade MO, Cook DJ, Guyatt GH, et al., Ventilation strategy using low tidal volumes, recruitment maneuvers, and high positive end-expiratory pressure for acute lung injury and acute respiratory distress syndrome: A randomized controlled trial, *JAMA* 299 (6) (2008) 637–645. [PubMed: 18270352]
- [151]. Terragni PP, Rosboch G, Tealdi A, Corno E, Menaldo E, Davini O, Gandini G, Herrmann P, Mascia L, Quintel M, Slutsky AS, Gattinoni L, Ranieri VM, Tidal Hyperinflation during Low Tidal Volume Ventilation in Acute Respiratory Distress Syndrome, *American Journal of Respiratory and Critical Care Medicine* 175 (2) (2007) 160–166. [PubMed: 17038660]
- [152]. Lowhagen K, Lundin S, Stenqvist O, Regional intratidal gas distribution in acute lung injury and acute respiratory distress syndrome—assessed by electric impedance tomography, *Minerva Anestesiol* 76 (12) (2010) 1024–1035. [PubMed: 21178912]
- [153]. Lowhagen K, Lindgren S, Odensjöd H, Stenqvist O, Lundin S, A new non-radiological method to assess potential lung recruitability: a pilot study in ALI patients, *Acta Anaesthesiologica Scandinavica* 55 (2) (2011) 165–174. [PubMed: 21039359]
- [154]. Pulletz S, Kott M, Elke G, Schädler D, Vogt B, Weiler N, Frerichs I, Dynamics of regional lung aeration determined by electrical impedance tomography in patients with acute respiratory distress syndrome, *Multidiscip Respiratory Medicine* 7 (1) (2012) 44.
- [155]. Long Y, Liu D-W, He H-W, Zhao Z-Q, Positive End-expiratory Pressure Titration after Alveolar Recruitment Directed by Electrical Impedance Tomography, *Chinese Medical Journal* 128 (11) (2015) 1421–1427. [PubMed: 26021494]
- [156]. Cinnella G, Grasso S, Raimondo P, DAntini D, Mirabella L, Rauseo M, Dambrosio M, Physiological Effects of the Open Lung Approach in Patients with Early, Mild, Diffuse Acute Respiratory Distress Syndrome: An Electrical Impedance Tomography Study, *Anesthesiology* 123 (5) (2015) 1113–1121. [PubMed: 26397017]

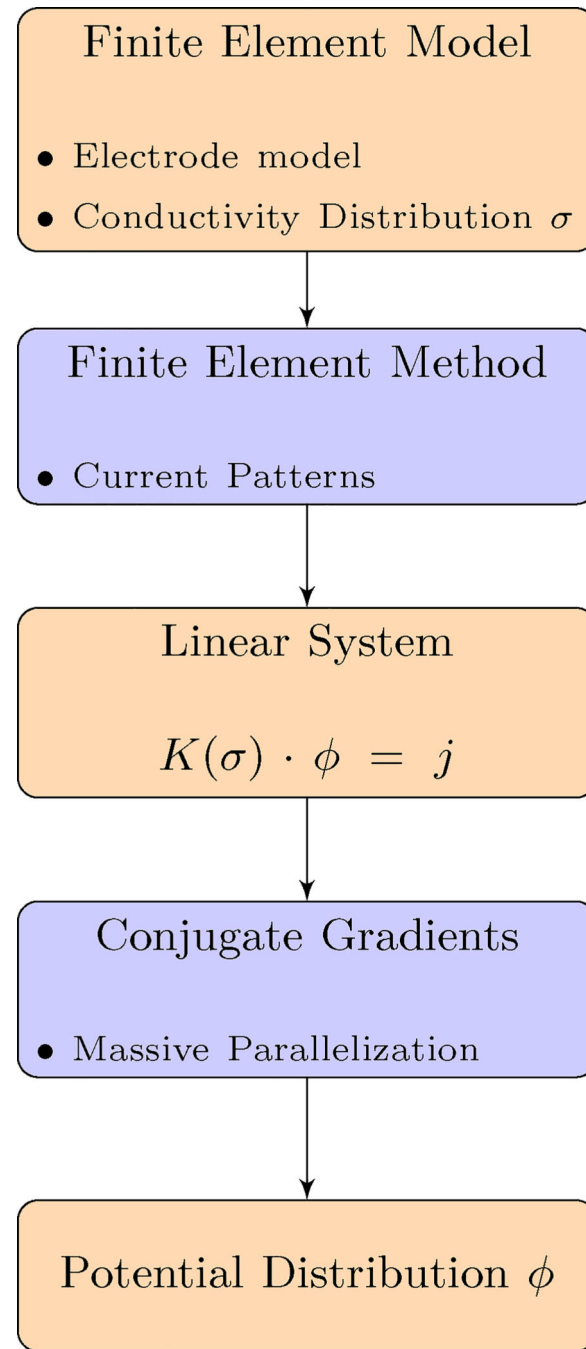
- [157]. Long Y, Huai-wu H, Knut M, Inz F, Dawei L, Zhanqi Z, Assessment of Lung Recruitment by Electrical Impedance Tomography and Oxygenation in ARDS Patients, *Medicine* 95 (22) (2016) e3820. [PubMed: 27258527]
- [158]. Franchineau G, Bréchot N, Lebreton G, Hekimian G, Nieszkowska A, Trouillet J-L, Leprince P, Chastre J, Luyt C-E, Combes A, Schmidt M, Bedside Contribution of Electrical Impedance Tomography to Setting Positive End-Expiratory Pressure for Extracorporeal Membrane Oxygenation-treated Patients with Severe Acute Respiratory Distress Syndrome, *American Journal of Respiratory and Critical Care Medicine* 196 (4) (2017) 447–457. [PubMed: 28103448]
- [159]. Eronia N, Mauri T, Maffezzini E, Gatti S, Bronco A, Alban L, Binda F, Sasso T, Marenghi C, Grasselli G, Foti G, Pesenti A, Bellani G, Bedside selection of positive end-expiratory pressure by electrical impedance tomography in hypoxicemic patients: a feasibility study, *Annals of Intensive Care* 7 (1) (2017) 76. [PubMed: 28730554]
- [160]. Spadaro S, Mauri T, Böhm SH, Scaramuzzo G, Turrini C, Waldmann AD, Ragazzi R, Pesenti A, Volta CA, Variation of poorly ventilated lung units (silent spaces) measured by electrical impedance tomography to dynamically assess recruitment, *Critical care (London, England)* 22 (1) (2018) 26.
- [161]. Heines SJH, Strauch U, van de Poll MCG, Roekaerts PMHJ, Bergmans DCJJ, Clinical implementation of electric impedance tomography in the treatment of ARDS: a single centre experience, *Journal of Clinical Monitoring and Computing*.
- [162]. Karagiannidis C, Waldmann AD, Róka PL, Schreiber T, Strassmann S, Windisch W, Böhm SH, Regional expiratory time constants in severe respiratory failure estimated by electrical impedance tomography: a feasibility study, *Critical Care* 22 (1) (2018) 221. [PubMed: 30236123]
- [163]. Krueger-Ziolek S, Schullcke B, Kretschmer J, Müller-Lisse U, Möller K, Zhao Z, Positioning of electrode plane systematically influences EIT imaging, *Physiological Measurement* 36 (6) (2015) 1109–1118. [PubMed: 26006327]
- [164]. Karsten J, Stueber T, Voigt N, Teschner E, Heinze H, Influence of different electrode belt positions on electrical impedance tomography imaging of regional ventilation: A prospective observational study, *Critical Care* 20 (1) (2016) 3. [PubMed: 26743570]
- [165]. Morais CCA, De Santis Santiago RR, Filho JRBO, Hirota AS, Pacce PHD, Ferreira JC, Camargo EDLB, Amato MBP, Costa ELV, Monitoring of Pneumothorax Appearance with Electrical Impedance Tomography during Recruitment Maneuvers, *American Journal of Respiratory and Critical Care Medicine* 195 (8) (2017) 1070–1073. [PubMed: 28409685]
- [166]. Gow C-H, Chang M-Y, Zhao Z, Möller K, Patient-ventilator asynchrony identified with electrical impedance tomography, *IFAC-PapersOnLine* 51 (27) (2018) 52–55.
- [167]. Wrigge H, Girrbach F, Hempel G, Detection of patient-ventilator asynchrony should be improved: and then what?, *Journal of thoracic disease* 8 (12) (2016) E1661–E1664. [PubMed: 28149608]
- [168]. Frerichs I, Hinz J, Herrmann P, Weisser G, Hahn G, Quintel M, Hellige G, Regional lung perfusion as determined by electrical impedance tomography in comparison with electron beam CT imaging, *IEEE Transactions on Medical Imaging* 21 (6) (2002) 646–652. [PubMed: 12166861]
- [169]. Borges JB, Suarez-Sipmann F, Bohm SH, Tusman G, Melo A, Maripuu E, Sandström M, Park M, Costa ELV, Hedenstierna G, Amato M, Regional lung perfusion estimated by electrical impedance tomography in a piglet model of lung collapse, *Journal of Applied Physiology* 112 (1) (2012) 225–236. [PubMed: 21960654]
- [170]. Pillow JJ, Frerichs I, Stocks J, Lung Function Tests in Neonates and Infants with Chronic Lung Disease: Global and Regional Ventilation Inhomogeneity, *Pediatric Pulmonology* 41 (2) (2006) 105–121. [PubMed: 16369918]
- [171]. Zhao Z, Fischer R, Mueller-Lisse U, Möller K, Ventilation inhomogeneity in patients with cystic fibrosis measured by electrical impedance tomography, 2012.
- [172]. Zhao Z, Müller-Lisse U, Frerichs I, Fischer R, Möller K, Regional airway obstruction in cystic fibrosis determined by electrical impedance tomography in comparison with high resolution CT, *Physiological Measurement* 34 (11) (2013) N107–N114. [PubMed: 24150032]

- [173]. Krueger-Ziolek S, Schullcke B, Zhao Z, Gong B, Naehrig S, Müller-Lisse U, Moeller K, Multi-layer ventilation inhomogeneity in cystic fibrosis, *Respiratory Physiology & Neurobiology* 233 (2016) 25–32. [PubMed: 27476932]
- [174]. Krueger-Ziolek S, Schullcke B, Gong B, Müller-Lisse U, Moeller K, EIT based pulsatile impedance monitoring during spontaneous breathing in cystic fibrosis, *Physiological Measurement* 38 (6) (2017) 1214–1225. [PubMed: 28530203]
- [175]. Wettstein M, Radlinger L, Riedel T, Effect of Different Breathing Aids on Ventilation Distribution in Adults with Cystic Fibrosis, *PLoS ONE* 9 (9) (2014) e106591.
- [176]. Eyübolu BM, Oner AF, Baysal U, Biber C, Keyf AI, Yilmaz U, Erdoan Y, Application of electrical impedance tomography in diagnosis of emphysema—a clinical study, *Physiological measurement* 16 (3 Suppl A) (1995) A191–211. [PubMed: 8528117]
- [177]. Vogt B, Zhao Z, Zabel P, Weiler N, Frerichs I, Regional lung response to bronchodilator reversibility testing determined by electrical impedance tomography in chronic obstructive pulmonary disease, *American Journal of Physiology-Lung Cellular and Molecular Physiology* 311 (1) (2016) L8–L19. [PubMed: 27190067]
- [178]. Frerichs I, Zhao Z, Becher T, Zabel P, Weiler N, Vogt B, Regional lung function determined by electrical impedance tomography during bronchodilator reversibility testing in patients with asthma, *Physiological Measurement* 37 (6) (2016) 698–712. [PubMed: 27203725]
- [179]. Vogt B, Löhr S, Zhao Z, Falkenberg C, Ankermann T, Weiler N, Frerichs I, Regional lung function testing in children using electrical impedance tomography, *Pediatric Pulmonology* 53 (3) (2018) 293–301. [PubMed: 29136345]
- [180]. Frerichs I, Achtzehn U, Pechmann A, Pulletz S, Schmidt EW, Quintel M, Weiler N, High-frequency oscillatory ventilation in patients with acute exacerbation of chronic obstructive pulmonary disease, *Journal of Critical Care* 27 (2) (2012) 172–181. [PubMed: 21715133]
- [181]. Sun Q, Liu L, Pan C, Zhao Z, Xu J, Liu A, Qiu H, Effects of neurally adjusted ventilatory assist on air distribution and dead space in patients with acute exacerbation of chronic obstructive pulmonary disease, *Critical care (London, England)* 21 (1) (2017) 126.
- [182]. Mauri T, Bellani G, Salerno D, Mantegazza F, Pesenti A, Regional Distribution of Air Trapping in Chronic Obstructive Pulmonary Disease, *American Journal of Respiratory and Critical Care Medicine* 188 (12) (2013) 1466–1467. [PubMed: 24328774]
- [183]. Brovman EY, Foley CA, Shen AH, Whang EE, Urman RD, Intraoperative Ventilation Patterns in Morbidly Obese Patients Undergoing Laparoscopic Bariatric Surgery, *Journal of Laparoendoscopic & Advanced Surgical Techniques* 28 (12) (2018) 1463–1470. [PubMed: 29870299]
- [184]. Wang W, Xu M-Y, Wu J-X, Zhao Z-Q, Influence of tidal volume on ventilation distribution and oxygenation during one-lungventilation, *The Kaohsiung Journal of Medical Sciences* 34 (7) (2018) 420–421. [PubMed: 30063016]
- [185]. Zhao Z, Wang W, Zhang Z, Xu M, Frerichs I, Wu J, Moeller K, Influence of tidal volume and positive end-expiratory pressure on ventilation distribution and oxygenation during one-lung ventilation, *Physiological Measurement* 39 (3) (2018) 034003. [PubMed: 29431700]
- [186]. Eichler L, Truskowska K, Dupree A, Busch P, Goetz AE, Zöllner C, Intraoperative Ventilation of Morbidly Obese Patients Guided by Transpulmonary Pressure, *Obesity Surgery* 28 (1) (2018) 122–129. [PubMed: 28707173]
- [187]. Nestler C, Simon P, Petroff D, Hammermüller S, Kamrath D, Wolf S, Dietrich A, Camilo LM, Beda A, Carvalho AR, Giannella-Neto A, Reske AW, Wrigge H, Individualized positive end-expiratory pressure in obese patients during general anaesthesia: a randomized controlled clinical trial using electrical impedance tomography, *British Journal of Anaesthesia* 119 (6) (2017) 1194–1205. [PubMed: 29045567]
- [188]. Radke OC, Schneider T, Vogel E, Koch T, Effect of Trigger Sensitivity on Redistribution of Ventilation During Pressure Support Ventilation Detected by Electrical Impedance Tomography, *Anesthesiology and pain medicine* 5 (4) (2015) e27439. [PubMed: 26478865]
- [189]. Hsu Y-L, Tien A-J, Chang M-Y, Chang H-T, Möller K, Frerichs I, Zhao Z, Regional ventilation redistribution measured by electrical impedance tomography during spontaneous breathing trial

- with automatic tube compensation, *Physiological Measurement* 38 (6) (2017) 1193–1203. [PubMed: 28294957]
- [190]. Zhao Z, Peng S-Y, Chang M-Y, Hsu Y-L, Frerichs I, Chang H-T, Möller K, Spontaneous breathing trials after prolonged mechanical ventilation monitored by electrical impedance tomography: an observational study, *Acta Anaesthesiologica Scandinavica* 61 (9) (2017) 1166–1175. [PubMed: 28832898]
- [191]. Karsten J, Grusnick C, Paarmann H, Heringlake M, Heinze H, Positive end-expiratory pressure titration at bedside using electrical impedance tomography in post-operative cardiac surgery patients, *Acta Anaesthesiologica Scandinavica* 59 (6) (2015) 723–732. [PubMed: 25867049]
- [192]. Schibler A, Pham TMT, Moray AA, Stocker C, Ventilation and cardiac related impedance changes in children undergoing corrective open heart surgery, *Physiological Measurement* 34 (10) (2013) 1319–1327. [PubMed: 24021191]
- [193]. Martins TC, Tsuzuki MSG, Investigating Anisotropic EIT with Simulated Annealing, IFAC-PapersOnLine 50 (1) (2017) 9961–9966.

**Figure 1:**

Inverse problem solution workflow. Inputs/outputs are shown in orange and processes are shown in blue. The mentioned methods (except for D-Bar) have a loop where the forward problem is iteratively evaluated. The objective function is calculated and the converge check is verified. If the convergence has not been reached, the solution is modified. The final conductivity distribution is obtained when the convergence is reached.

**Figure 2:**

The forward problem is explained. Inputs/outputs are shown in orange and processes are shown in blue. The finite element model has the electrode model and the conductivity distribution  $\sigma$ . The FEM has as input the finite element model and the current patterns. A sparse linear system is created and it is solved using the CG algorithm, and the potential distribution  $\phi$  is determined. The CG algorithm is implemented using massive parallelization. The output is a set of electric potentials.

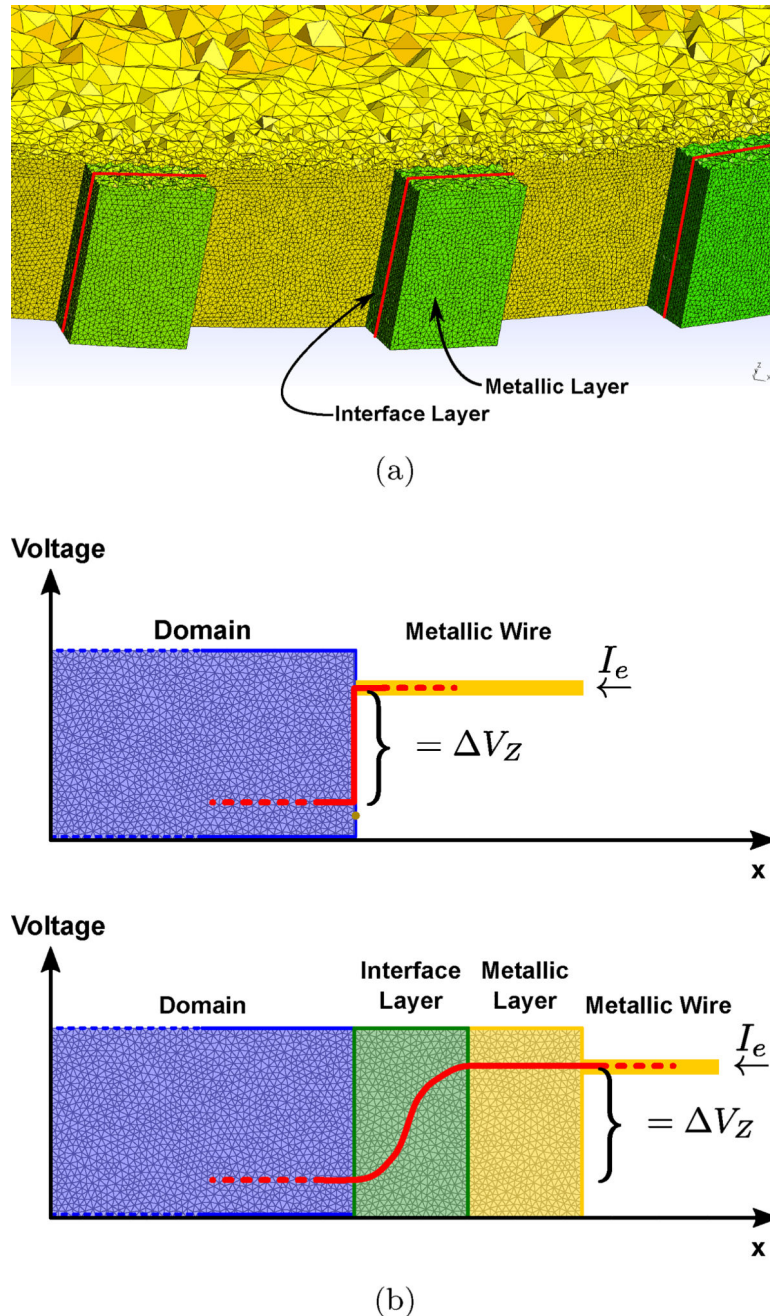


**Figure 3:**  
3D mesh for multi-layer electrode model [50]. (a) FE mesh detail of electrode layers. (b) Potential drop at interface layer due to contact impedance  $Z = V_Z I_e$ . Top: theoretical potential drop. Bottom: gradual potential drop due to interface layer.

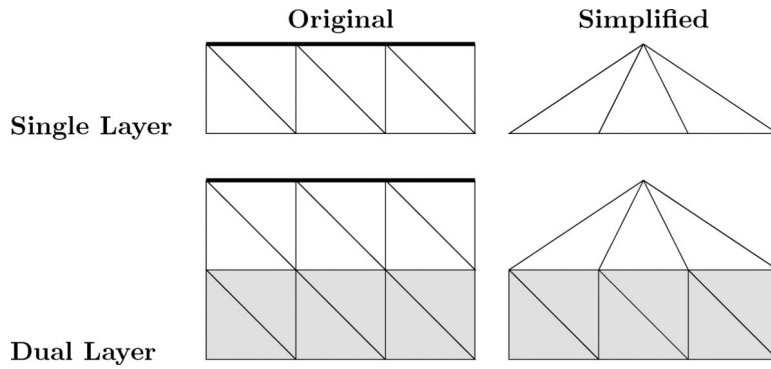


**Figure 4:**  
Representation of 2D single and double layer electrode model.

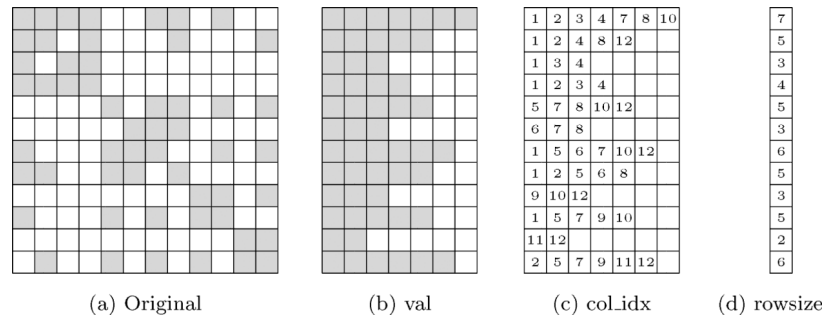
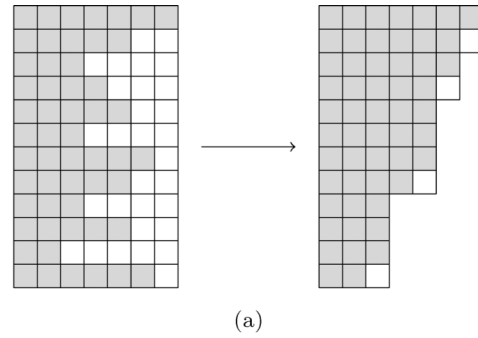


**Figure 5:**  
ELLPACK-R representation example.



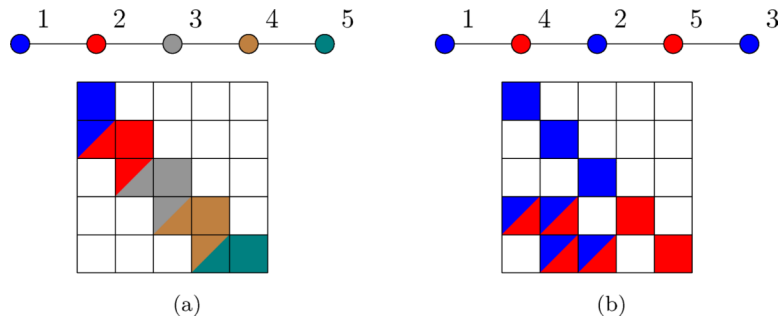
(a)

val:	[	1	2	3	4	7	8	10	1	5	6	7	10	12	2	5	7	9	11	12	1	2	4	8	12	5	7	8	]
		10	12	1	2	5	6	8	1	5	7	9	10	1	2	3	4	1	3	4	6	7	8	9	10	12	11	12	
col_idx:	[	7	6	6	5	5	5	4	3	3	3	2	]																
rowsize:	[	1	8	15	21	27	32	37	42	47	50	53	56	]															
col_offset:	[	1	7	12	2	5	8	10	4	3	6	9	11	]															
permvec:	[	1	7	12	2	5	8	10	4	3	6	9	11	]															

(b)

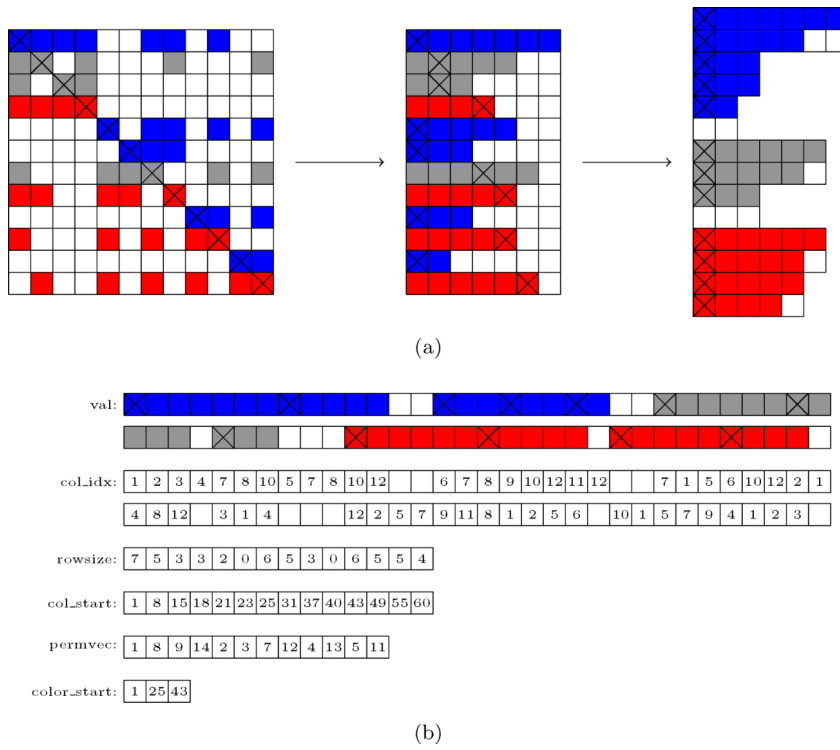
**Figure 6:**

pJDS format example with a warp size of 2. (a) Conversion from ELLPACK-R to pJDS and (b) its vector representation.

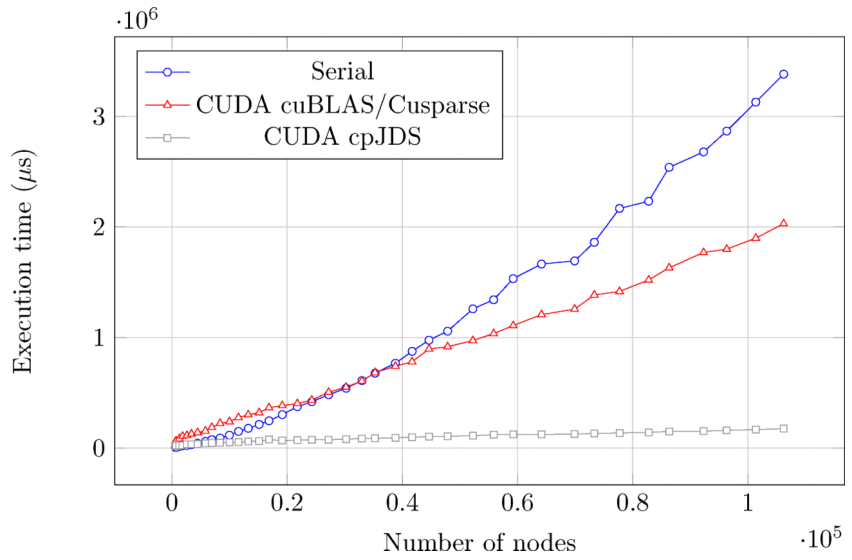


**Figure 7:**

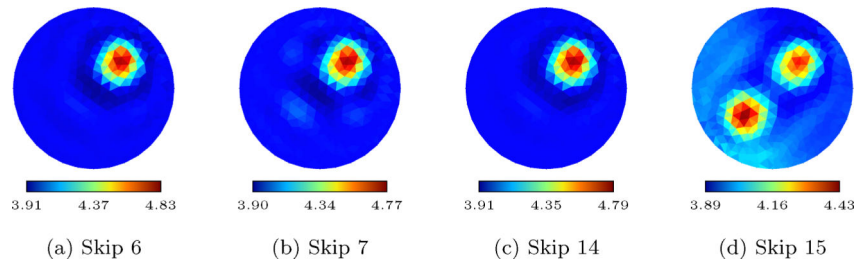
Coloring and reorder impact on the triangular solver parallelization. (a) Original system. (b) Node reordering generating a compatible system for parallelization.



**Figure 8:**  
cpJDS format example with a warp size of 2. (a) Conversion from ELLPACK-R to cpJDS and (b) its vector representation.

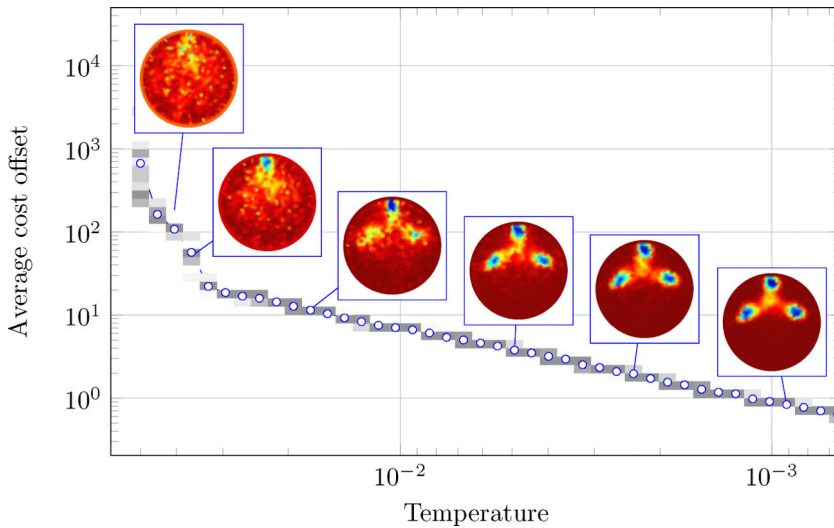


**Figure 9:**  
Execution times for the forward solvers.



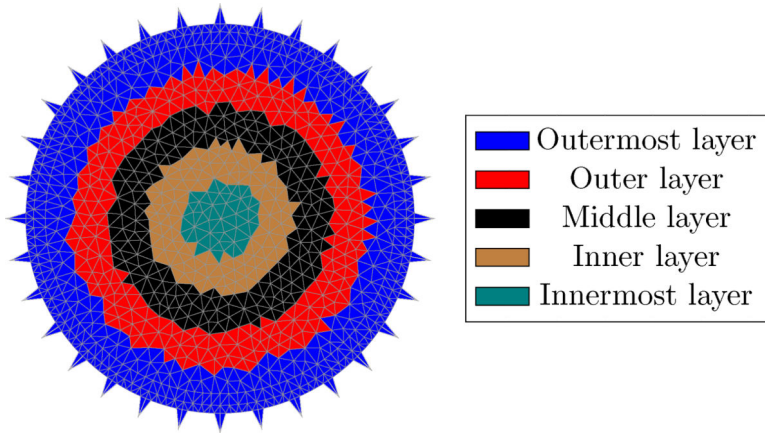
**Figure 10:**

Reconstructions of a numerically simulated 3D cylinder. The current injection pattern and the differential measurement were (a) skip 6, (b) skip 7, (c) skip 14 and (d) skip 15. Notice that (d) has an artifact, the rank of the observability matrix is the smaller.



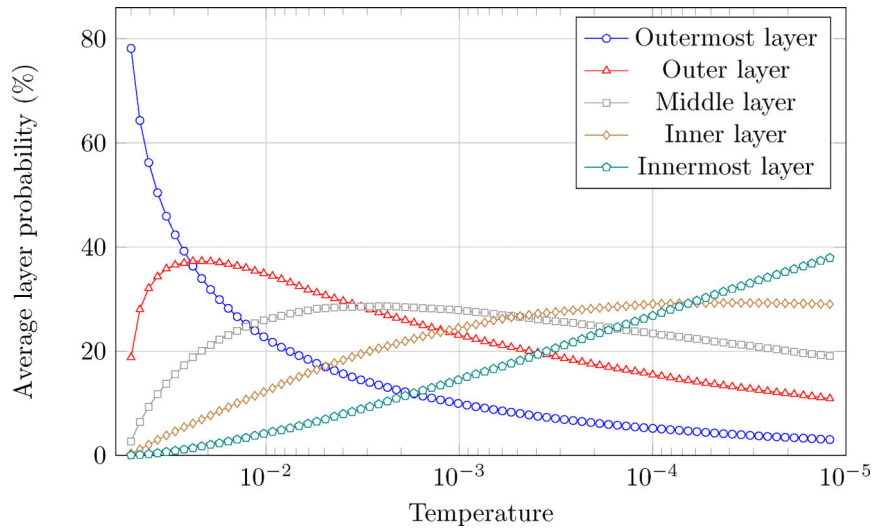
**Figure 11:**

Convergence of EIT reconstruction showing the outside-in property emerged from the SA-CG. The gray-scale histogram represents the cost distribution for each temperature step.



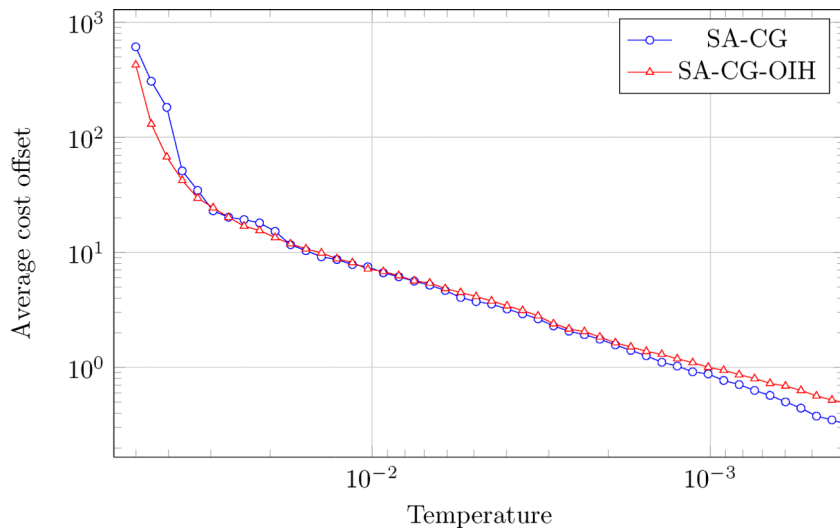
**Figure 12:**

Layers for the outside-in heuristic used by the SA-CG-OIH.



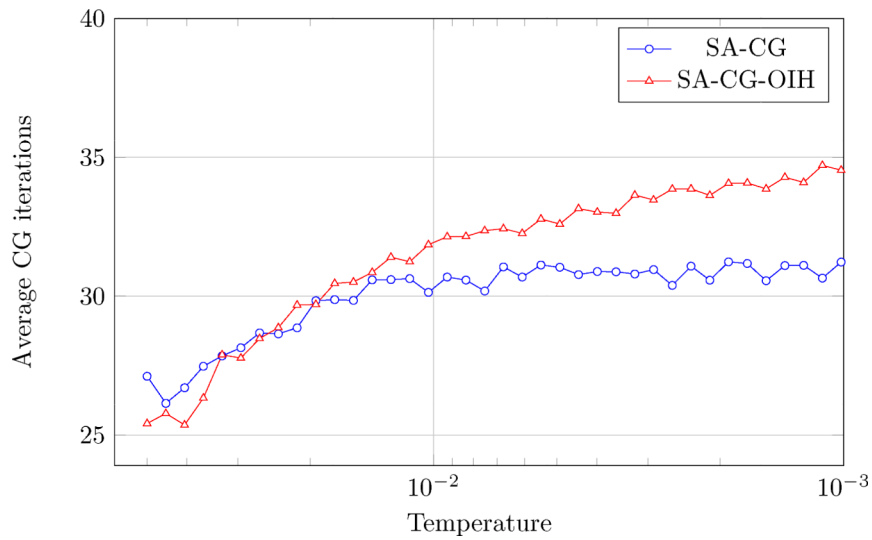
**Figure 13:**

Layer probabilities for the outside-in heuristic used with the SA-CG-OIH. One might observe that the probabilities decrease for external layers as the temperature decreases, and the opposite happens for inner layers. This is the outside-in heuristic.

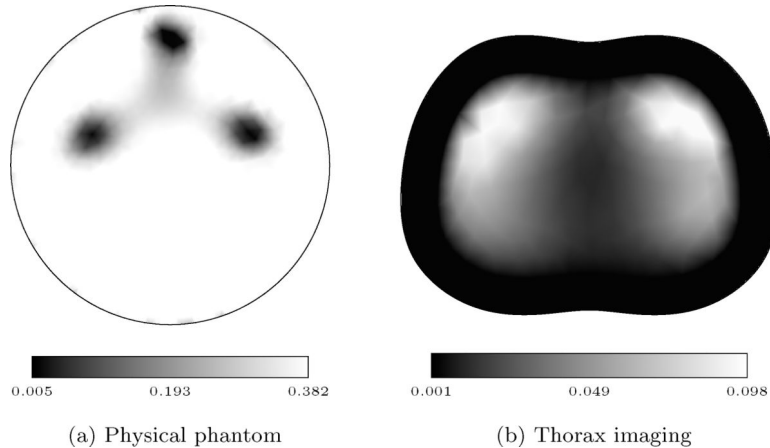


**Figure 14:**

Average objective function for each temperature. The graph indicates that the outside-in heuristic contributes to a faster convergence when compared with the conventional SA-CG, mainly at initial temperatures.

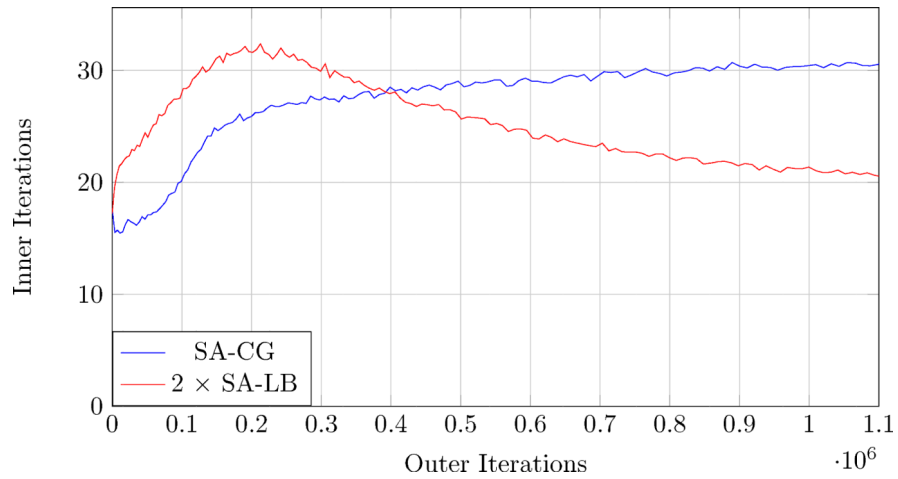
**Figure 15:**

Average CG iterations per temperature comparing the conventional SA-CG and the SA-CG-OIH. Note that the mesh used has 1, 024 nodes, requiring 1, 024 iterations to completely solve the linear system; however, only a maximum of 35 iterations is averagely performed for each temperature.



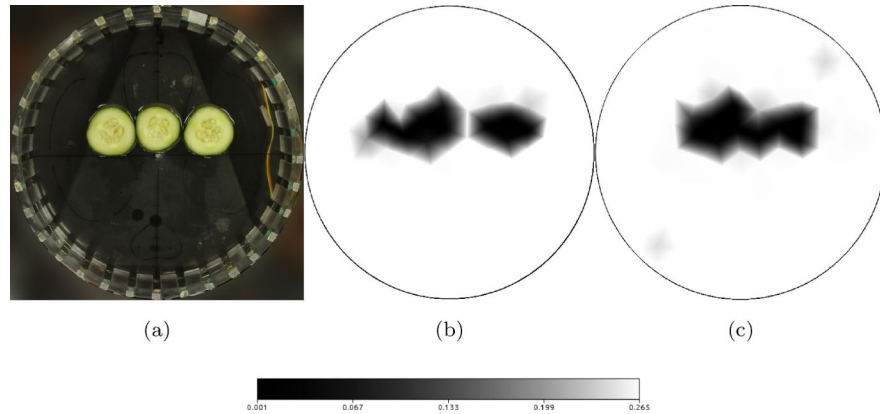
**Figure 16:**

EIT reconstructions (conductivity distribution in  $(\Omega \cdot m)^{-1}$ ) using the proposed method: (a) physical phantom experiment. (b) a thorax application.



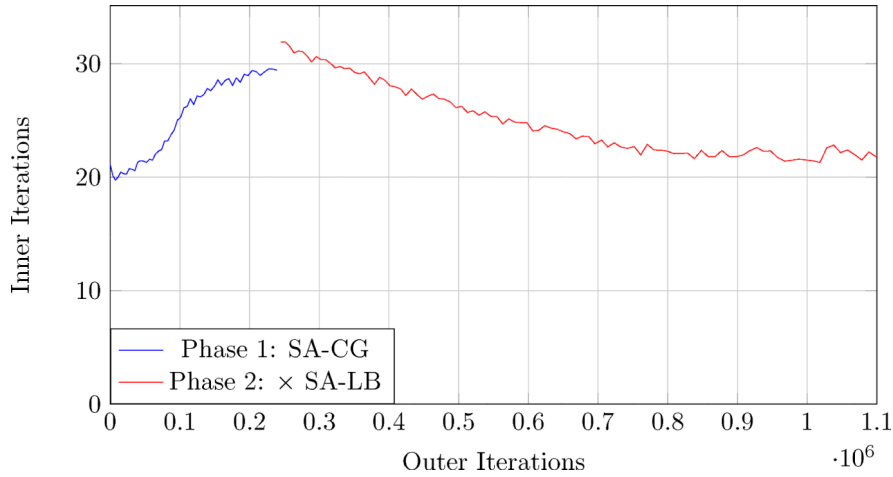
**Figure 17:**

Inner Iterations  $\times$  Outer Iterations, for SA-CG and SA-LB (the cost of each SA-LB inner iteration is roughly the cost of two SA-CG inner iterations). As both SA methods have different temperature scales, the SA outer iteration is used instead.



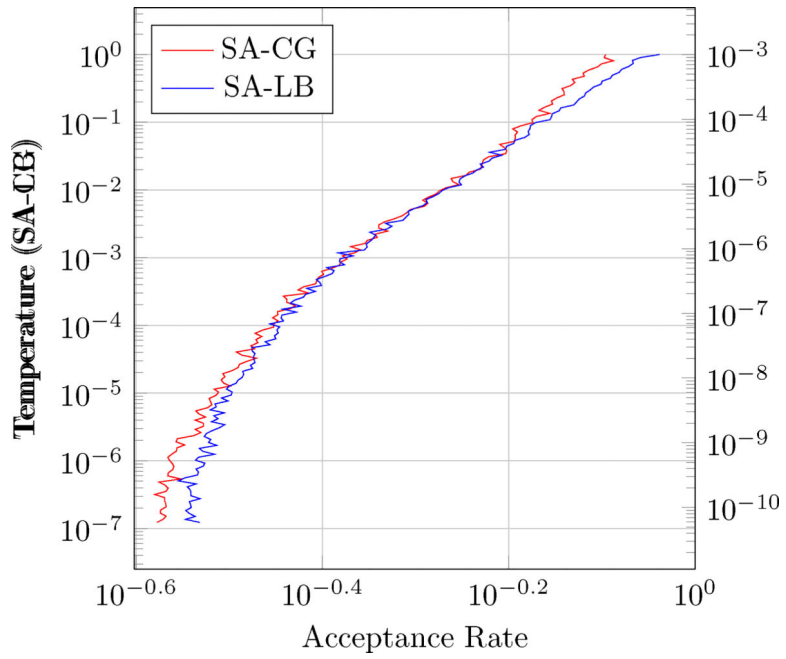
**Figure 18:**

(a) “Dash” phantom and its coarse reconstructions using (b) SA-CG and (c) SA-LB.  
Conductivity values are in  $(\Omega \cdot \text{m})^{-1}$ .



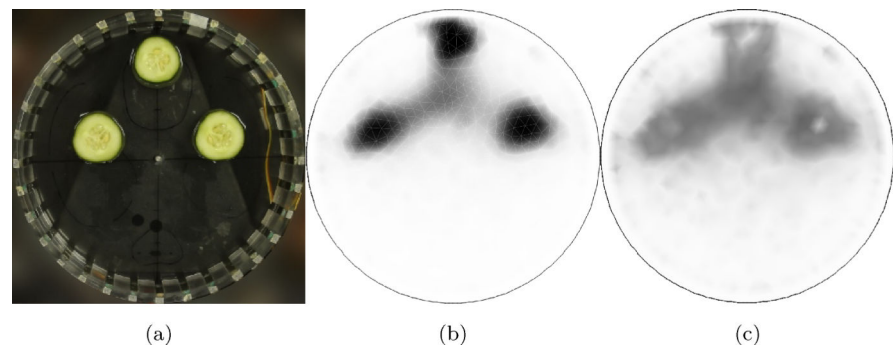
**Figure 19:**

Inner Iterations  $\times$  Outer Iterations, for the two-steps reconstruction.



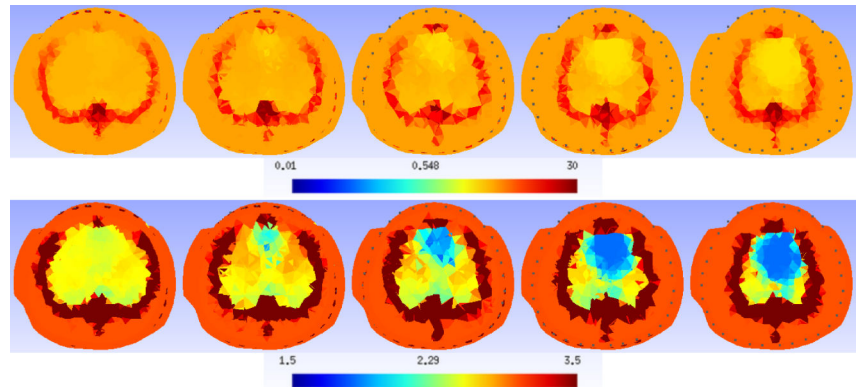
**Figure 20:**

Temperature  $\times$  rejection rate for both SA-CG and SA-LB objective functions.

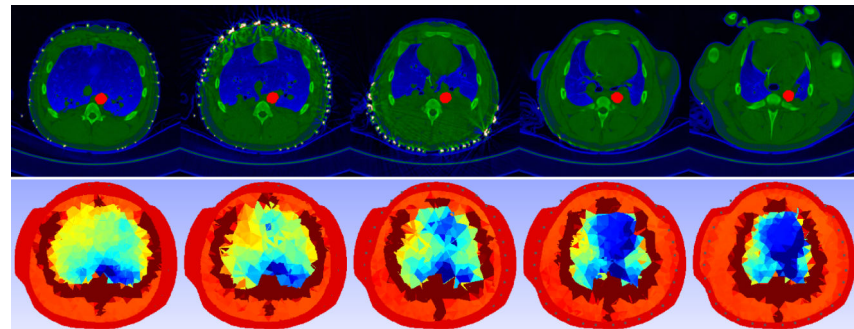


**Figure 21:**

(a) “Triangle” phantom and its average image (b) and standard variance (c).

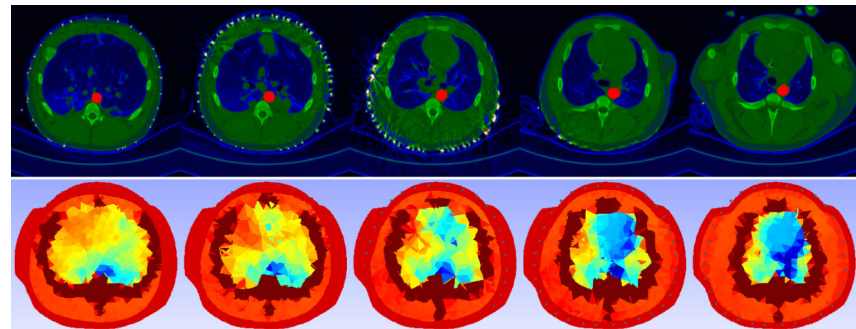
**Figure 22:**

Mean resistivity image at 5 different levels obtained from the anatomical atlas, with 2 different color scales (top:  $0.01 \rho 30\Omega.m$ ; bottom:  $1.5 \rho 3.5\Omega.m$ ).



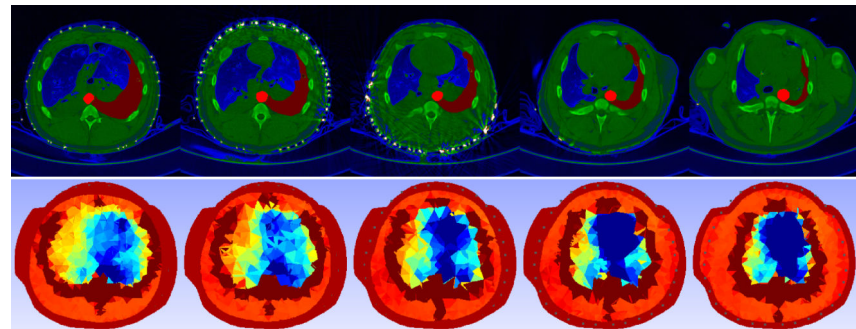
**Figure 23:**

Top: CT image of swine ventilated with PEEP of  $5\text{cmH}_2\text{O}$  at 5 different levels. The aorta is marked in light red. Bottom: respective resistivity image obtained with G-N method using anatomical atlas ( $1.5 \quad \rho \quad 3.5\Omega.\text{m}$ ).



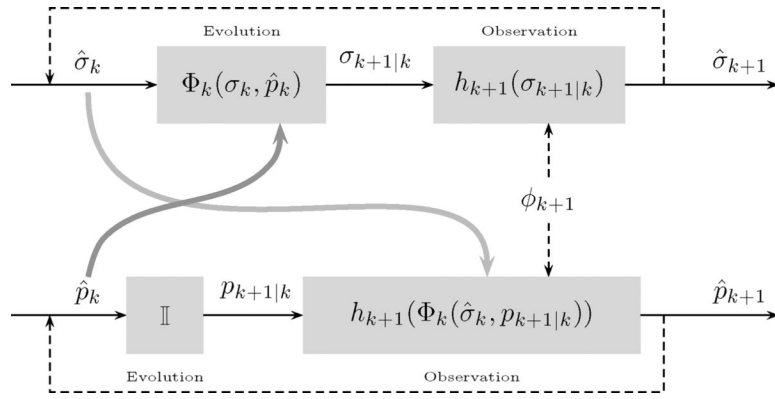
**Figure 24:**

Top: CT image of swine ventilated with PEEP of  $25 \text{ cm H}_2\text{O}$  at 5 different levels. The aorta is marked in light red. Bottom: respective resistivity image obtained with G-N method using anatomical atlas ( $1.5 \leq \rho \leq 3.5 \Omega \cdot \text{m}$ ).

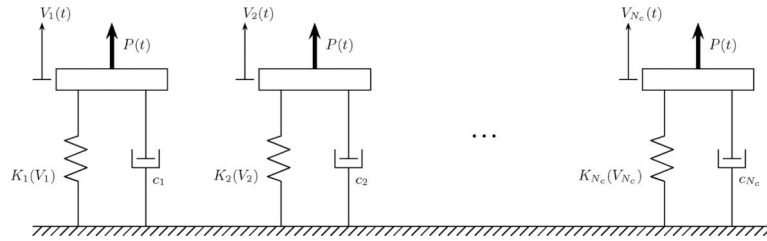


**Figure 25:**

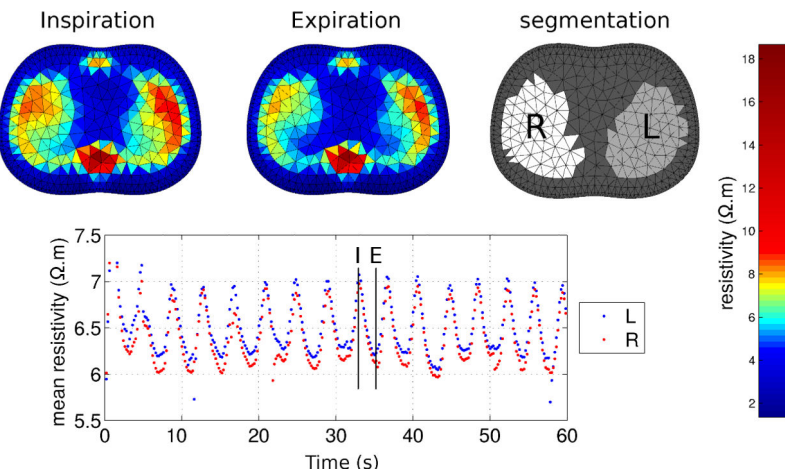
Top: CT image of swine ventilated with PEEP of  $12 \text{ cm H}_2\text{O}$ , with pleural effusion (marked in dark red) on the left side of the thoracic chest, at 5 different levels. The aorta is marked in light red. Bottom: respective resistivity image obtained with G-N method using anatomical atlas ( $1.5 \leq \rho \leq 3.5\Omega$ ).

**Figure 26:**

Dual estimation using Kalman filter. Two Kalman filters run in parallel.

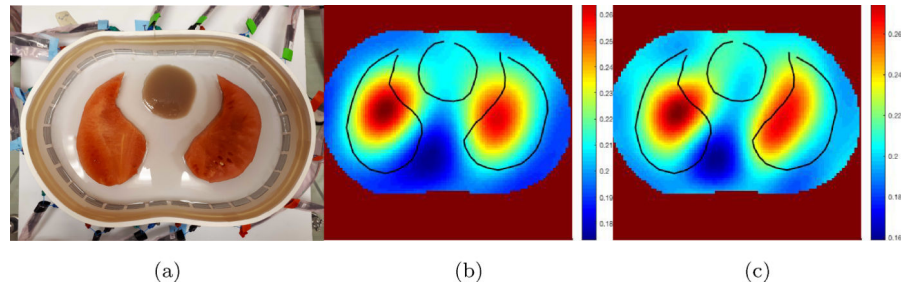


**Figure 27:**  
Representation of the pulmonary dynamic model.



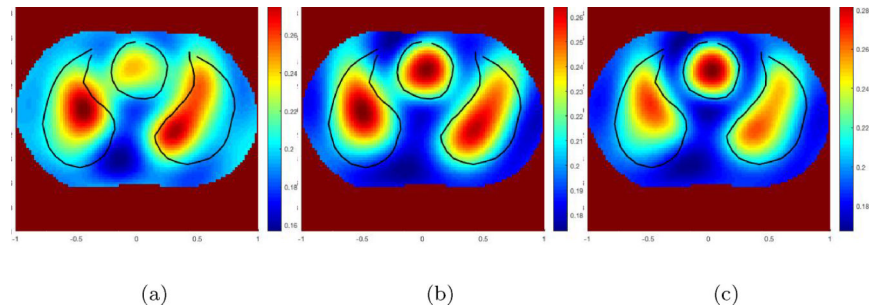
**Figure 28:**

Resistivity estimation using the Kalman filter. Top: two representative images from peak inspiration (I) and expiration (E) and the compartments of the model, identified by the segmentation algorithm(L/R). Bottom: average resistivity of each compartment as a function of discrete time  $T_s = 0.02s$ .

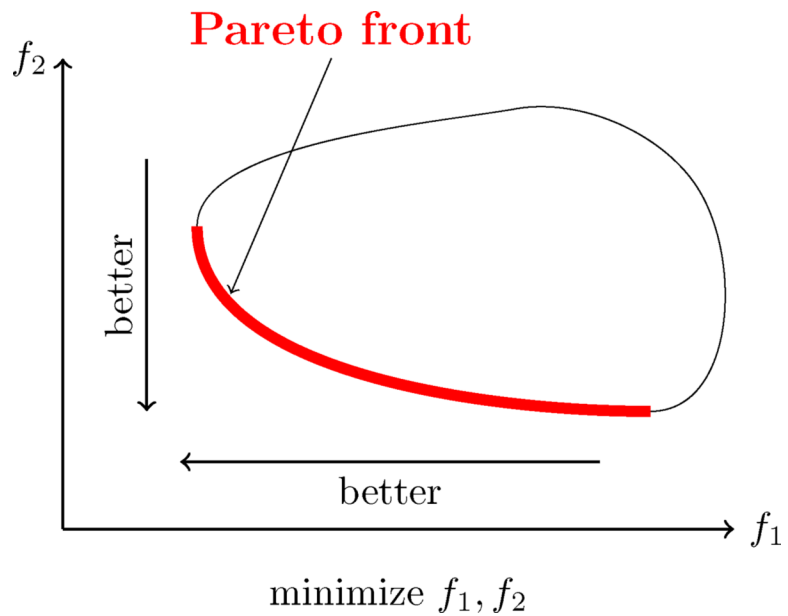


**Figure 29:**

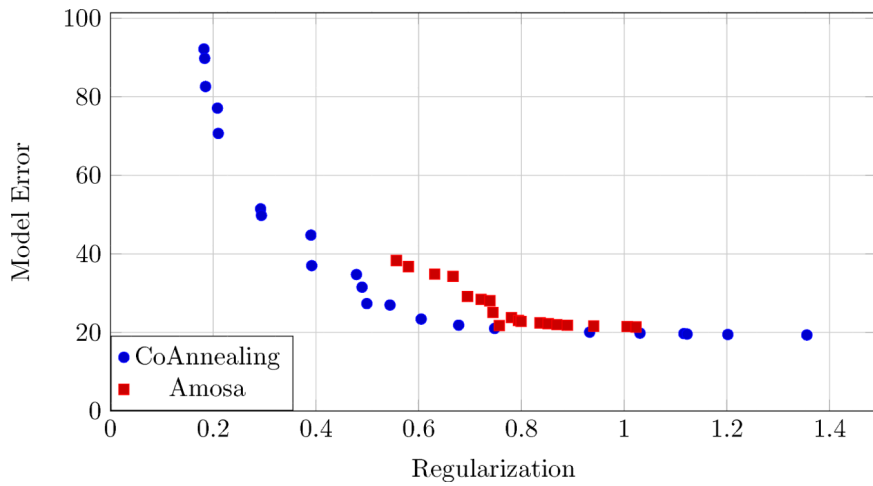
(a) Phantom with agar heart and melon lungs (b) Absolute image using the D-bar algorithm with the  $t^{\text{exp}}$  approximation with maximum truncation radius  $R = 5$  and (c)  $R = 6$ . Conductivity values are in mS/m.

**Figure 30:**

(a) Absolute image using the D-bar method and a weak prior ( $\alpha = 0.75, R_1 = 6, R_2 = 7$ ) (b) a second weak prior ( $\alpha = 0.75, R_1 = 5, R_2 = 6$ ) and (c) a moderate prior ( $\alpha = 0.5, R_1 = 5, R_2 = 8$ ). Conductivity values are in mS/m.

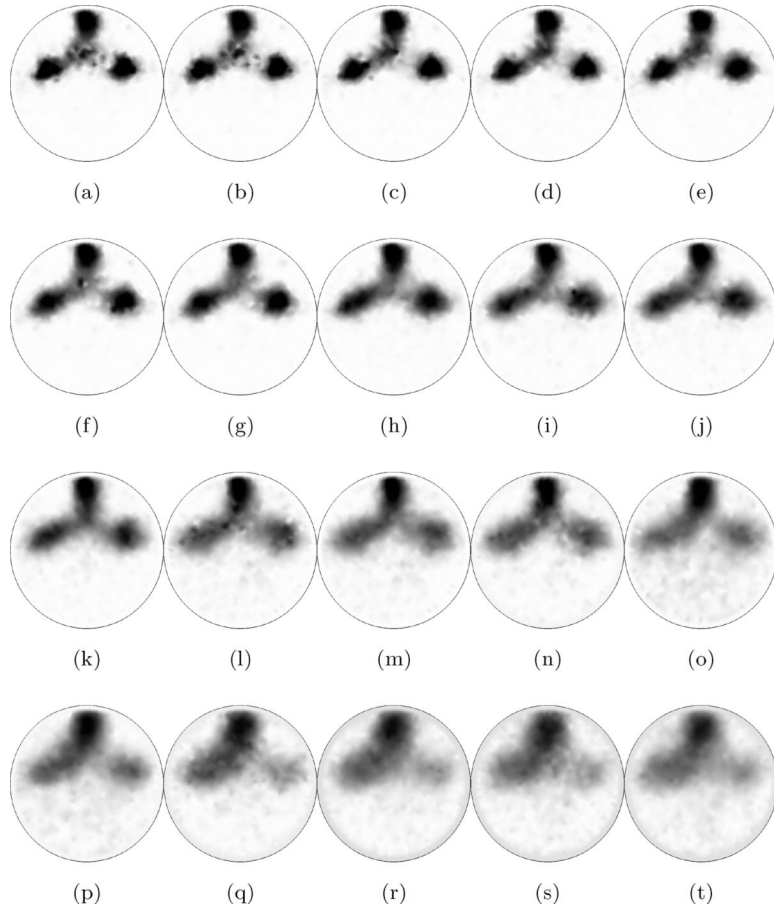


**Figure 31:**  
Pareto front to a bi-objective minimization problem.



**Figure 32:**

Pareto front comparison of CoAnnealing (in blue) and AMOSA (in red).

**Figure 33:**

Solutions within the pareto front. As regularization value decreases, so are the high-frequency components of the reconstructed image. For less regularized images (a)-(e), there are reconstruction artifacts imposed by the mesh. On higher regularized images (p)-(t), the image loses definition and it hinders the visualization of the 3 cucumber slices.